The S6 gate in regulatory Kv6 subunits restricts heteromeric K+ channel stoichiometry

Aditya Pisupati[1,2] , Keith J. Mickolajczyk[3], William Horton[4] , Damian B. van Rossum[5,6], Andriy Anishkin[7] , Sree V. Chintapalli[8], Xiaofan Li[1] , Jose Chu-Luo[1], Gregory Busey[1] , William O. Hancock[3], and Timothy Jegla[1,9]

The Shaker-like family of voltage-gated K+ channels comprises four functionally independent gene subfamilies, Shaker (Kv1), Shab (Kv2), Shaw (Kv3), and Shal (Kv4), each of which regulates distinct aspects of neuronal excitability. Subfamily-specific assembly of tetrameric channels is mediated by the N-terminal T1 domain and segregates Kv1–4, allowing multiple channel types to function independently in the same cell. Typical Shaker-like Kv subunits can form functional channels as homotetramers, but a group of mammalian Kv2-related genes (Kv5.1, Kv6s, Kv8s, and Kv9s) encodes subunits that have a "silent" or "regulatory" phenotype characterized by T1 self-incompatibility. These channels are unable to form homotetramers, but instead heteromerize with Kv2.1 or Kv2.2 to diversify the functional properties of these delayed rectifiers. While T1 self-incompatibility predicts that these heterotetramers could contain up to two regulatory (R) subunits, experiments show a predominance of 3:1R stoichiometry in which heteromeric channels contain a single regulatory subunit. Substitution of the self-compatible Kv2.1 T1 domain into the regulatory subunit Kv6.4 does not alter the stoichiometry of Kv2.1:Kv6.4 heteromers. Here, to identify other channel structures that might be responsible for favoring the 3:1R stoichiometry, we compare the sequences of mammalian regulatory subunits to independently evolved regulatory subunits from cnidarians. The most widespread feature of regulatory subunits is the presence of atypical substitutions in the highly conserved consensus sequence of the intracellular S6 activation gate of the pore. We show that two amino acid substitutions in the S6 gate of the regulatory subunit Kv6.4 restrict the functional stoichiometry of Kv2.1:Kv6.4 to 3:1R by limiting the formation and function of 2:2R heteromers. We propose a two-step model for the evolution of the asymmetric 3:1R stoichiometry, which begins with evolution of self-incompatibility to establish the regulatory phenotype, followed by drift of the activation gate consensus sequence under relaxed selection to limit stoichiometry to 3:1R.

Introduction

Shaker-like Kv channels regulate neuronal excitability, including many aspects of action potential repolarization and timing. The Shaker-like Kv gene family consists of four functionally independent subfamilies, which provide a diverse array of depolarization-gated K+ currents: Shaker (Kv1), Shab (Kv2), Shaw (Kv3) and Shal (Kv4; Wei et al., 1990; Covarrubias et al., 1991). Many of the delayed rectifier and transient A-type currents observed in neurons are encoded by Shaker-like Kv family genes, and some of their most notable roles are described below. Kv1 channels localize to the axon initial segment and juxtaparanodes of mammalian neurons, where they participate in axonal action potential repolarization (Wang et al., 1993; Dodson et al., 2002;

Ogawa et al., 2008; Trimmer, 2015). They appear to underlie the classical delayed rectifier of the squid giant axon (Rosenthal et al., 1996). Kv2 channels encode the majority of somatodendritic delayed rectifiers (Tsunoda and Salkoff, 1995b; Murakoshi and Trimmer, 1999; Du et al., 2000; Malin and Nerbonne, 2002; Misonou et al., 2005), but they can also be found in ankyrin-free zones of the axon initial segment in mammalian neurons (King et al., 2014). Mammalian Kv3 channels underlie rapid high threshold delayed rectifiers that facilitate high spike rates in fast-firing neurons (Wang et al., 1998; Lau et al., 2000; Rudy and McBain, 2001; Lien and Jonas, 2003). Kv4 channels, in contrast, encode classical somatodendritic A-currents found in many mammalian

[1]Department of Biology, Pennsylvania State University, University Park, PA;   [2]Medical Scientist Training Program, College of Medicine, Pennsylvania State University, Hershey, PA;   [3]Department of Biomedical Engineering, Pennsylvania State University, University Park, PA;   [4]Department of Animal Science, Pennsylvania State University, University Park, PA;   [5]The Jake Gittlen Laboratories for Cancer Research, College of Medicine, Pennsylvania State University, Hershey, PA;   [6]Division of Experimental Pathology, Department of Pathology, College of Medicine, Pennsylvania State University, Hershey, PA;   [7]Department of Biology, University of Maryland, College Park, MD;   [8]Arkansas Children's Nutrition Center and Department of Pediatrics, University of Arkansas for Medical Sciences, Little Rock, AR;   [9]Huck Institutes of the Life Sciences, Pennsylvania State University, University Park, PA.

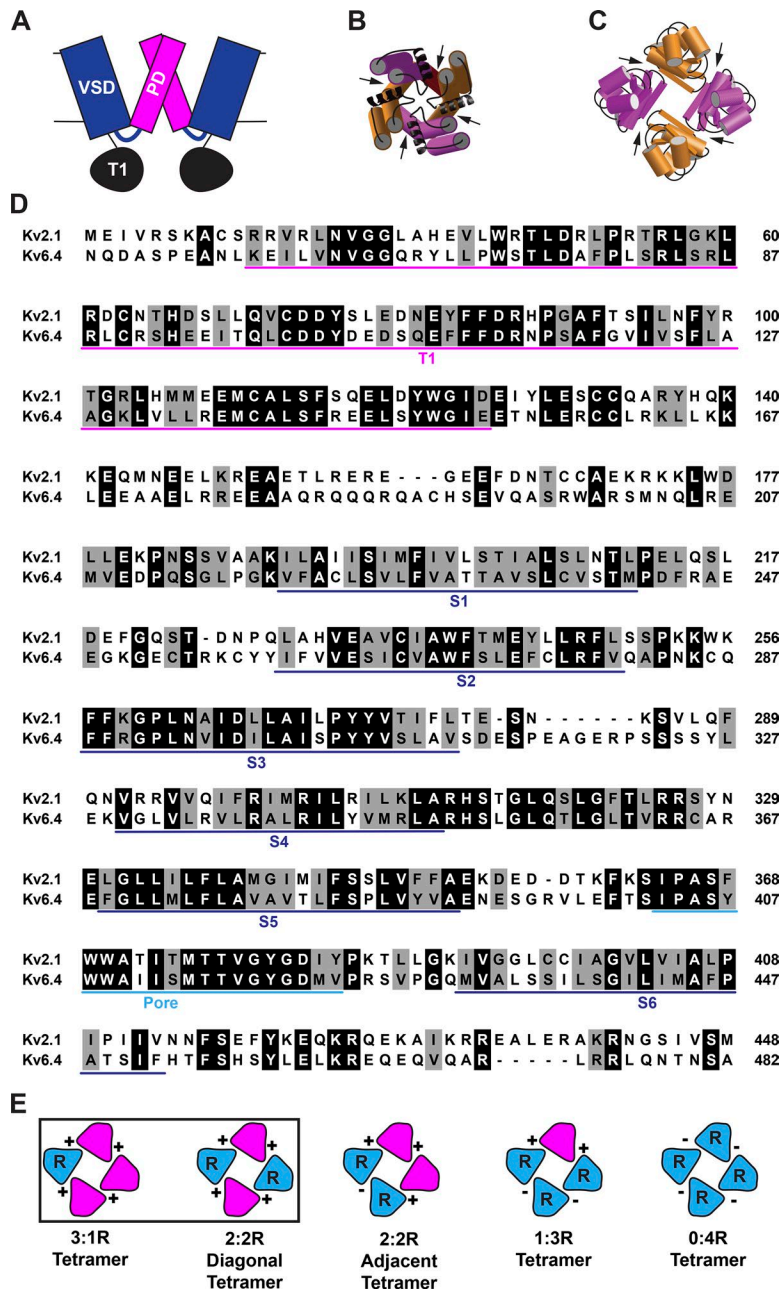Correspondence to Timothy Jegla: tjj3@psu.edu.

Figure 1. Tetrameric Shaker-like Kv channels have two major intersubunit interfaces. (A) Schematic cartoon depicting subunit domain arrangement in Shaker-like Kv channels. Two diagonally opposed subunits of the tetrameric channel are shown. The PDs (magenta) from each subunit surround a central ion-conducting pore, while the VSDs (blue) are physically isolated at the periphery. The conserved N-terminal cytoplasmic assembly domains (T1, black) form a ring beneath the pore. **(B)** A more detailed cartoon of the tetrameric ion conducting pore from an extracellular perspective, with adjacent subunits differentially shaded. Transmembrane helices S5 and S6 are depicted with cylinders, and a selectivity filter helix is shown as a black ribbon. The pore-lining S6 helix forms a major intersubunit interface (arrows), and the intracellular side comprises the activation gate. **(C)** Cartoon of the cytoplasmic T1 ring with adjacent subunits differentially shaded. There are major intersubunit contacts between neighboring, but not diagonally opposed, T1s (arrows). Helices are depicted with cylinders, and β-sheets are depicted with rectangles. **(D)** Amino acid alignment of mouse Kv2.1 and Kv6.4 with residue numbers given at the right margin. Identical residues are shaded black, and conservative substitutions are shaded gray. The T1 domain is underlined in magenta, transmembrane domains S1–S6 are underlined in dark blue, and the PD is underlined in light blue. The alignment was produced with the CLUSTALW algorithm as implemented in MEGA7 (Kumar et al., 2016), and un-conserved N and C termini have been trimmed. **(E)** T1 self-incompatibility in regulatory subunits (blue) theoretically allows formation of heterotetramers with a single (3:1R) or two diagonally opposed (2:2R) regulatory subunits because four compatible T1 contacts (+ signs) remain in each case. However, T1 self-incompatibility rules out formation of 2:2R with adjacent regulatory subunits, 1:3R and 4R tetramers, all of which have at least one incompatible intersubunit contact (minus signs).

and invertebrate neurons (Tsunoda and Salkoff, 1995a; Malin and Nerbonne, 2000, 2001; Carrasquillo and Nerbonne, 2014), although it should be noted that Kv1 subfamily channels can contribute a kinetically distinct component to somatodendritic A-type currents in at least some mammalian neurons (Malin and Nerbonne, 2001; Carrasquillo and Nerbonne, 2014).

Shaker-like Kv channels are tetrameric (MacKinnon, 1991; Long et al., 2005a), with each subunit containing a canonical voltage-gated cation channel core motif of six transmembrane domains (S1–S6). S1–S4 comprise the voltage sensor domain (VSD), while S5–S6 comprise the pore domain (PDs) with the K+ selectivity filter formed on the extracellular side by a highly conserved loop (Jiang et al., 2003; Long et al., 2005a,b). Each channel has four spatially independent VSDs, but a single pore formed by extensive intersubunit contact between the PDs. The unique and defining feature of Shaker-like Kvs relative to other voltage-gated K+ channels is the presence of a cytoplasmic N-terminal domain, T1, which promotes assembly of tetramers and forms another large intersubunit interface (Shen and Pfaffinger, 1995; Xu et al., 1995; Kreusch et al., 1998; Long et al., 2005a). Fig. 1, A–D, summarizes the structural layout of tetrameric Shaker-like Kv channels, including the two major intersubunit interfaces in T1 and the inner pore. T1-mediated tetramer assembly requires physical interaction between neighboring T1 domains and is subfamily-specific because T1s from distinct subfamilies are not compatible and do not interact (Shen and Pfaffinger, 1995; Xu et al., 1995). The T1 domain therefore plays a key role in maintaining functional segregation of the Kv1, Kv2, Kv3, and Kv4 subfamilies.

Kv1–4 subunits can typically assemble as functional homotetramers, and the isolated T1 domain is itself able to self-assem-

Pisupati et al.
Kv6.4 S6 gate influences K+ channel stoichiometry

Journal of General Physiology
https://doi.org/10.1085/jgp.201812121

1703

ble into a tetrameric structure (Pfaffinger and DeRubeis, 1995; Kreusch et al., 1998). A notable exception to this rule of assembly is a group of ten "silent" or "regulatory" subunits discovered in mammals, Kv5.1, Kv6.1–6.4, Kv8.1–8.2, and Kv9.1–9.3, that are self-incompatible and thus not able to form homotetramers, but can form functional heteromeric channels with novel biophysical properties when coexpressed with Kv2.1 or Kv2.2 (Post et al., 1996; Patel et al., 1997; Salinas et al., 1997a,b; Kramer et al., 1998; Zhu et al., 1999; Ottschytsch et al., 2002). While the names of these channels imply that they belong to distinct gene subfamilies, phylogenetic analysis places them within the Kv2 subfamily (Jegla et al., 2012; Li et al., 2015b), thus preserving the principle of subfamily-specific assembly. In the absence of Kv2.1, Kv6.4 regulatory subunits do not assemble into tetramers and do not traffic to the plasma membrane (Ottschytsch et al., 2002, 2005). Mammalian regulatory subunit T1s also do not oligomerize in vitro, suggesting T1 self-incompatibility plays a significant role in generation of the self-incompatible regulatory subunit phenotype (Salinas et al., 1997b; Kramer et al., 1998; Ottschytsch et al., 2002).

Crystal structures of Shaker channels show that a T1 domain only physically interacts with T1s from neighboring subunits; there is no interaction between T1s of diagonally opposed subunits (Kreusch et al., 1998; Long et al., 2005a). T1 self-incompatibility of regulatory subunits therefore predicts that regulatory subunits could combine with Kv2.1 in two possible channel stoichiometries: (1) an asymmetric stoichiometry with three Kv2.1s and a single regulatory subunit (3:1R), or (2) a symmetric stoichiometry with two Kv2.1s and two diagonally opposed regulatory subunits (2:2R; Fig. 1 E). T1 self-incompatibility rules out 1:3R channels and 2:2R channels with adjacent regulatory subunits, but in theory would not be able to distinguish between a 3:1R or diagonal 2:2R stoichiometry. However, FRET-based determination of the Kv2.1:Kv9.3 stoichiometry suggests that heteromers form predominantly in the asymmetric 3:1R stoichiometry (Kerschensteiner et al., 2005). Measurements of gating charge components attributable to Kv6.4 and Kv2.1 support a 3:1R stoichiometry for Kv2.1:Kv6.4 heteromers (Bocksteins et al., 2017), and therefore suggest that the 3:1R stoichiometry might be shared among mammalian Kv2 family regulatory subunits.

We reasoned there must be additional factors beyond T1 self-incompatibility of regulatory subunits that bias formation of functional channels in the 3:1R stoichiometry. There is indeed evidence suggesting that T1 self-incompatibility is not the only factor guiding assembly of regulatory subunits. For instance, substitution of the Kv2.1 T1 into Kv6.4 is not sufficient to restore assembly of functional homomeric channels (Ottschytsch et al., 2005), and N terminus/C terminus interaction may play a role in blocking the ability of Kv6.4 to assemble with Kv3 channels (Bocksteins et al., 2014). To find channel regions that might be responsible for determining regulatory subunit stoichiometry, we used an evolutionary approach to look for regulatory subunit sequence signatures near the two major subunit interfaces in Shaker-like Kv family tetramers, the T1 contacts and the PD contacts. T1-containing Shaker-like Kvs can be traced to a common ancestor of all extant metazoans (Li et al., 2015b), and diversification of voltage-gated K+ channels (including the Shaker-like Kv, KCNQ, and EAG families) into the functional classes, or sub-

families, found in vertebrates occurred before the divergence of bilaterians and cnidarians (Jegla and Salkoff, 1994, 1997; Jegla et al., 1995, 2012; Sand et al., 2011; Martinson et al., 2014; Li et al., 2015b,c). Kv1–Kv4 channels can all be found in cnidarians, and the functional properties of all four subfamilies, including subfamily-specific assembly, are highly conserved between cnidarians and bilaterians. Most important for this study, the regulatory subunit phenotype evolved independently in cnidarians in the Kv1, Kv3, and Kv4 subfamilies (Jegla and Salkoff, 1997; Jegla et al., 2012; Li et al., 2015b), providing a rich dataset for identification of regulatory subunit sequence signatures.

We show here that alteration of the highly conserved sequence of the pore's intracellular activation gate is a universal signature for evolution of the regulatory subunit phenotype. The activation gate forms part of the interface between subunits (Fig. 1 B), and extensive mutagenesis studies of Shaker subfamily channels have demonstrated that various substitutions in the gate can block channel maturation, interfere with gating, and alter conductance (Hackos et al., 2002; Kitaguchi et al., 2004; Pau et al., 2017). We tested the hypothesis that these gate substitutions could play a role in determining the stoichiometry of heteromeric channels containing regulatory subunits using a combination of TIRF microscopy and electrophysiology.

Materials and methods

Molecular cloning

Mouse Kv2.1 and Kv6.4 cDNA were isolated from whole brain mRNA using RT-PCR, cloned into pOX plasmid (Jegla and Salkoff, 1997) using HindIII/XbaI (Kv2.1) or EcoR1/Xba1 (Kv6.4), and the sequence was confirmed to code proteins identical to Refseq (Kv2.1, NP_032446; Kv6.4, NP_080010). Kv6.4-Kv2.1T1, Kv6.4-PIPIIV-Kv2.1CT, and Kv6.4-PIPIIV chimeras were generated from two PCR fragments using standard overlap PCR techniques and cloned into pOX using EcoR1/Xba1. For the Kv6.4-Kv2.1T1 chimera, the following primers were used: piece 1 (Kv2.1 T1), 5′-TAT AGAATTCCACCATGCCGGCGGGCAT-3′ (sense) and 5′-AGCCTC CTCCCGGCGCAGCGTCTCAGCC-3′ (antisense), and piece 2 (Kv6.4 core to C terminus), 5′-AGGCTGAGACGCTGCGCCGGGAGGAGG-3′ (sense) and 5′-TCTCTCTAGAGTGGTGGGAGTTACAT-3′ (antisense). Kv6.4-PIPIIV-Kv2.1CT was generated with the following primers: piece 1 (Kv6.4 upstream of gate), 5′-TCTCGAATTCCA CCATGCCCATGTCT-3′ (sense) and 5′-GTTATTGACGATAATTGG AATTGGGA-3′ (antisense), and piece 2 (Kv2.1 gate through C terminus), 5′-CTTATCATGGCTTTCCCAATTCCAATT-3′ (sense) and 5′-TCTCTCTAGATTCAGATACTCTGATCC-3′ (antisense). Kv6.4-PIPIIV was generated in the same manner except using a piece 2 containing the Kv6.4 C terminus generated with the following primers: 5′-TCATGCCTTTCCCAATTCCAATTATCG-3′ (sense) and 5′-TCTCTCTAGAGTGGTGGGAGTTACAT-3′ (antisense). Kv6.4-Kv2.1CT, Kv6.4-PITIIV-Kv2.1CT, Kv6.4-PIPIIF-Kv2.1CT, and Kv6.4-PITIIF-Kv2.1CT were generated by cloning PCR fragments into Kv6.4-PIPIIV-Kv2.1CT using an internal BamH1 site in S6 upstream of the gate and Xba1. Fragments were generated using the antisense primer 5′-TCTCTCTAGATTCAGATACTCTGATCC-3′ and the following sense primers: 5′-AGCGGGATCCTTATCATG GCTTTCCCAGCCACATCCATCTTCCACACCTTCTCCGAGTTCTAC-

3′ (Kv6.4-Kv2.1CT); 5′-AGCGGGATCCTTATCATGGCTTTCCCAATT ACAATTATCGTCAATAAC-3′ (Kv6.4-PITIIV-Kv2.1CT); 5′-AGCGGG ATCCTTATCATGGCTTTCCCAATTCCAATTATCTTCAATAACTTC TC-3′ (Kv6.4-PIPIIF-Kv2.1CT); and 5′-AGCGGGATCCTTATCATG GCTTTCCCAATTACAATTATCTTCAATAACTTCTC-3′ (Kv6.4-PIT IIF-Kv2.1CT). Pore cysteine mutants for Cd^{2+} block experiments were constructed using the QuikChange protocol (Wang and Malcolm, 1999) with the following primers: Kv2.1 I383C, (sense) 5′-GTTGGTTACGGAGACTGCTACCCTAAGACTCTCCTG-3′ and (antisense) 5′-CAGGAGAGTCTTAGGGTAGCAGTCTCCGTAACC AAC-3′; Kv6.4 M422C (sense) 5′-GTGGGCTATGGGGACTGCGTC CCTCGCAGCGTCCCG-3′ and (antisense) 5′-CGGGACGCTGCG AGGGACGCAGTCCCCATAGCCCAC-3′. Enhanced GFP (Zhang et al., 1996) tags were cloned onto the N terminus of Kv2.1- or Kv6.4-based constructs using NheI/HindIII or NheI/EcoRI, respectively. The flexible linkers between the GFP tag and channel N termini were QQQAST for Kv2.1 and QQQNST for Kv6.4. Oligonucleotide primers were obtained from IDT (Integrated DNA Technologies), and all constructs were confirmed by sequencing.

Complementary RNA (cRNA) synthesis and *Xenopus* oocyte preparation

For all constructs, capped cRNAs were made by run-off transcription from NotI-linearized templates using the T3 mMessage mMachine kit (Life Technologies). Prior to injection, cRNA was purified using lithium chloride precipitation and analyzed by gel electrophoresis for integrity. cRNAs were stored at –80°C and diluted to the desired concentration for injection in a 1:20 mix of the RNase inhibitor SUPERase-In (Invitrogen) and nuclease-free water. Optimal amounts of cRNA for injection were empirically determined for each batch of cRNA. Mature stage V/VI *Xenopus laevis* oocytes were injected with 50 nl of cRNA using a NanoJect II injector (Drummond Scientific). Defolliculated oocytes were isolated from *X. laevis* ovaries (*Xenopus* 1) using collagenase digestion (Type II Collagenase; Sigma Aldrich), as previously described (Clancy et al., 2009) and maintained at 18°C in an oocyte culture solution consisting of 98 mM NaCl, 2 mM KCl, 1.8 mM $CaCl_2$, 1 mM $MgCl_2$, 5 mM HEPES, 2.5 mM Na-pyruvate, 100 U/ml penicillin, and 100 µg/ml streptomycin, pH 7.2.

Electrophysiology

Two-electrode voltage clamp (TEVC) recordings for biophysical characterization of heteromers and expression ratio titrations used the following bath solution: 96 mM NaOH, 2 mM NaCl, 2 mM KCl, 1 mM $CaCl_2$, 1 mM $MgCl_2$, and 5 mM HEPES, pH 7.0, using methanesulfonic acid. For Cd^{2+} block experiments, the following base solution was used: 100 mM LiCl, 2 mM $CaCl_2$, 1 mM $MgCl_2$, and 5mM HEPES, pH 7.4. A LiCl-based solution has previously been found to optimize Cd^{2+} block for rat Kv2.1 I379C, the equivalent of mouse Kv2.1 I384C used here for Cd^{2+} block experiments (Krovetz et al., 1997). All chemicals were obtained from Sigma-Aldrich. Glass electrodes (1–3 MΩ) were pulled using a P-1000 Flaming/Brown Micropipette Puller (Sutter Instruments) and filled with 3 M KCl. Oocytes were clamped using a Dagan CA-1B amplifier and the pClamp 10 acquisition software for data collection and analysis (Molecular Devices). Data were sampled at 10 kHz and low-pass-filtered at 2 kHz using a four-pole Bessel filter.

Voltage-activation (GV) curves were determined from isochronal tail currents recorded after test pulses. Tail currents were fit with a single Boltzmann: $G(V) = \left[(A1 - A2)/\left(1 + e^{(V-V_{50})/dx}\right)\right] + A2$, where G is the conductance at voltage V, $A1$ is the initial value, $A2$ is the final value, V_{50} is the midpoint and dx is the slope factor. Reported V_{50} and slope factor values are the mean ± SEM of fits from individual oocytes, and data were normalized before averaging for display. Steady-state inactivation (SSI) data were determined from peak currents measured during a test pulse to +40 mV following prepulses to varying voltages and fit with the same equation. Non-inactivating pedestal current fractions were defined as $A2/A1$.

The procedure for data collection for the cRNA expression ratio titrations shown in Fig. 8 was developed in a series of pilot titration experiments to identify conditions that minimized inter-oocyte variation in current size, the optimal time window for a recording session, and the optimal amount of Kv2.1 cRNA to provide sufficient dynamic range for quantification while minimizing the chance of nonspecific current suppression. Batch-to-batch variation in current size is significant and required a single batch of oocytes to be used for each of the final cRNA titration experiments. We estimated that 15–20 µA of current was needed in the control Kv2.1 oocyte recordings in order to adequately resolve Kv6.4-dependent loss in current. We injected the minimum amount of Kv2.1 cRNA required to reach this level in ~36 h of incubation at 18°C (0.47 ng/oocyte); oocytes were tested for expression level, and experiments were performed when optimal expression was reached. Because of the low amount of Kv2.1 cRNA needed, total cRNA injected never exceeded 50 ng/oocyte even at the most Kv6.4-biased expression ratios. This is below the 50–100 ng of cRNA we injected to maximize expression in oocytes for patch clamp analysis (Jegla et al., 2012; Li et al., 2015a). We and others have observed preservation of subfamily-specific dominant negative suppression for Shaker-like channels and hyperpolarization-activated cation channels with ≥50 ng total cRNA and ≥20 µA total current (Xue et al., 2002; Li et al., 2015b). It is therefore unlikely that current loss observed in the expression titration experiments here is due to nonspecific suppression related to channel expression level and trafficking or oocyte toxicity. Data for the RNA titration experiments in Fig. 8 were normalized to the average peak current in control Kv2.1 oocytes from the same recording session. Each RNA titration experiment lasted ~4–6 h. To neutralize the effect of small changes in channel expression over this period of time, recordings from oocytes expressing distinct cRNA ratios were interleaved.

For the Cd^{2+}-block experiments in Fig. 9, peak current before Cd^{2+} exposure served as an internal control for each individual oocyte. Current size after Cd^{2+} exposure was normalized to this control before data averaging. Because each oocyte has an internal control, the timing of recordings post-injection did not need to be tightly synchronized as for the titration experiment described above. Data from two different batches of oocytes were pooled for each condition.

For on-cell patch recordings of single channels, recordings were made 1–3 d postinjection, and cRNAs were diluted ≥10-fold more than for TEVC recordings. Kv2.1 and Kv6.4 were injected at ratios suitable to observe both homomeric and heteromeric cur-
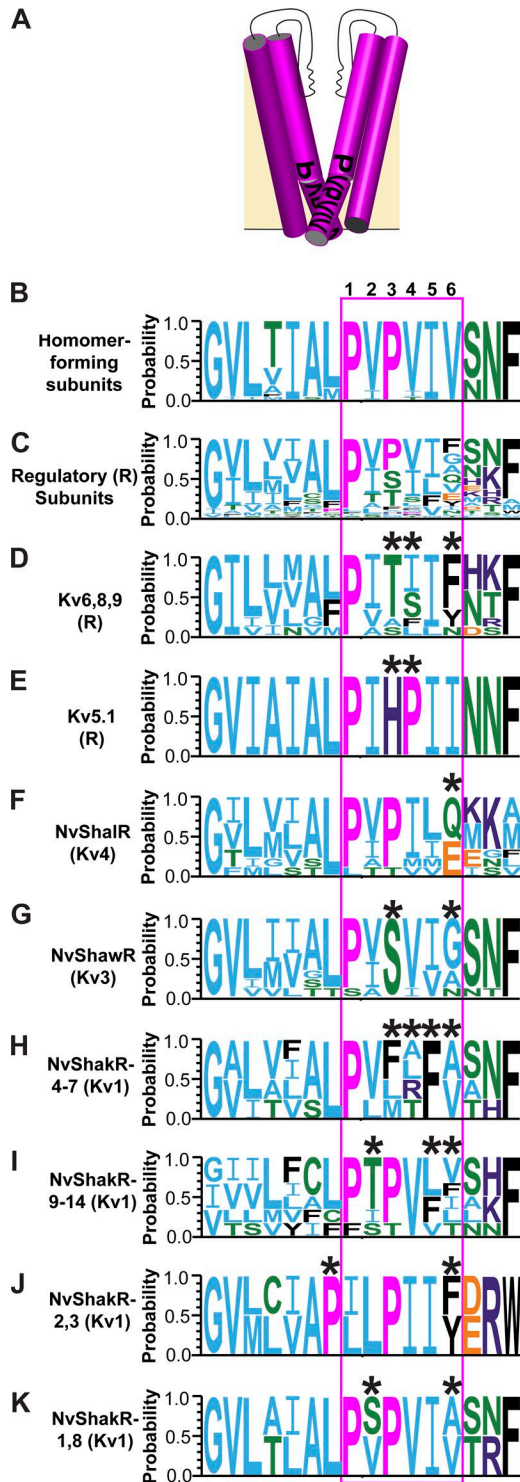
Figure 2. **The S6 activation gate sequence differs from the Shaker-like Kv family consensus in evolutionarily independent regulatory subunit groups. (A)** Cartoon showing the PD of two diagonally opposed subunits of a closed Shaker-like Kv channel tetramer with the location of a six–amino acid sequence (PVPVIV) comprising the S6 gating hinge and activation gate overlaid to show its approximate location at the intracellular side of the conduction pathway. **(B)** S6 consensus sequence logo constructed from all 27 mouse and sea anemone (*N. vectensis*) Shaker-like Kv family subunits that can form functional homotetrameric channels. The hinge and activation gate are boxed with a red outline, and positions 1–6 as used in the paper are indicated. A highly conserved section of S6 upstream of the gate is also shown in the

rents as determined by TEVC (see Fig. 8 H). Vitelline membranes of oocytes were mechanically removed as previously described (Li et al., 2015a) and transferred to a recording dish filled with internal solution (138 mM KMES, 4 mM KCl, 10 mM HEPES, 5 mM EGTA, pH 7.2; MES). Patch pipettes (0.4–1 MΩ) were coated with Sticky Wax (Kerr Dental Laboratory Products), fire-polished, and filled with a solution containing 140 mM KMES, 2 mM KCl, 1 mM $MgCl_2$, 0.2 mM $CaCl_2$, and 10 mM HEPES, pH 7.2. Ground was isolated with a 1 M NaCl agarose bridge, junction potential was canceled before patch formation, and pipette capacitance was compensated. Data were collected using a Multiclamp 700A amplifier and the pClamp 9 acquisition package (Molecular Devices). Data were sampled at 20 kHz and filtered at 1.4 kHz.

TIRF microscopy

Prior to imaging, oocyte vitelline envelopes were mechanically removed, and stripped oocytes were mounted on Number 0 Coverslips (VWR) in a custom-made chamber filled with oocyte culture solution. Care was taken to place the stripped oocyte onto the chamber such that the animal pole faces the microscope objective; this was done to limit autofluorescence during movie acquisition. The chamber was loaded onto a Nikon TE-2000 inverted microscope outfitted with a 60× numerical aperture 1.45 objective (Nikon). An 80-mW argon ion laser (Spectra Physics) was used for illumination, and a Cascade 512B electron-multiplying charge-coupled device (Roper Scientific) was used for detection. 240-s movies were acquired at 5 frames per second using MetaVue software (Molecular Devices). TIRF experiments were performed within 12–18 h after injection, and cRNAs were diluted 2–10-fold more than for electrophysiology to achieve optimal channel density. To ensure sufficient numbers of analyzable photobleaching spots, at least three movies were obtained for each egg, and photobleaching data were obtained for three to six different eggs from two to four different batches of oocytes for each GFP-tagged construct.

TIRF photobleaching data were analyzed in a semi-automated manner using a custom MATLAB (Mathworks) script. Briefly, fluorescence intensity over time traces for well-isolated spots were acquired from tagged image file format (TIFF) stacks, which summed counts in a 7-pixel diameter circle drawn around candi-

logo. Amino acid frequency is encoded in letter height, and colors are used to depict amino acid class (blue, hydrophobic; green, hydrophilic; magenta, proline; black, aromatic; orange, acidic; purple, basic). Note the conservative substitution V2I and V4I are found in mouse Kv2.1 and Kv2.2 and are typical for the Kv2 subfamily. **(C)** A similar sequence logo constructed from 43 mouse and sea anemone Shaker-like Kv regulatory subunits shows degeneration of the gate PVPVIV consensus sequence; only P1 is found in a majority of regulatory subunits. **(D)** Sequence logo for nine mouse Kv2 subfamily regulatory subunits with a common evolutionary origin (Kv6.1-6.4, Kv8.1-8.2, Kv9.1-9.3). Asterisks mark positions with unusual substitutions in at least some members of the group. Note the loss of P3 (hydroxyl typical) and V6 (aromatic typical) across the group. **(E–K)** Sequence logos broken out for seven additional evolutionarily independent groups of mouse and sea anemone regulatory subunits. Each separate group of regulatory subunits has a distinct pattern of unusual gate substitutions, marked by asterisks. Accession numbers and sequences for channels used to make the sequence logos in B–E are given in Supplemental Table 1, and amino acid frequencies at each gate position are given in Supplemental Table 2.
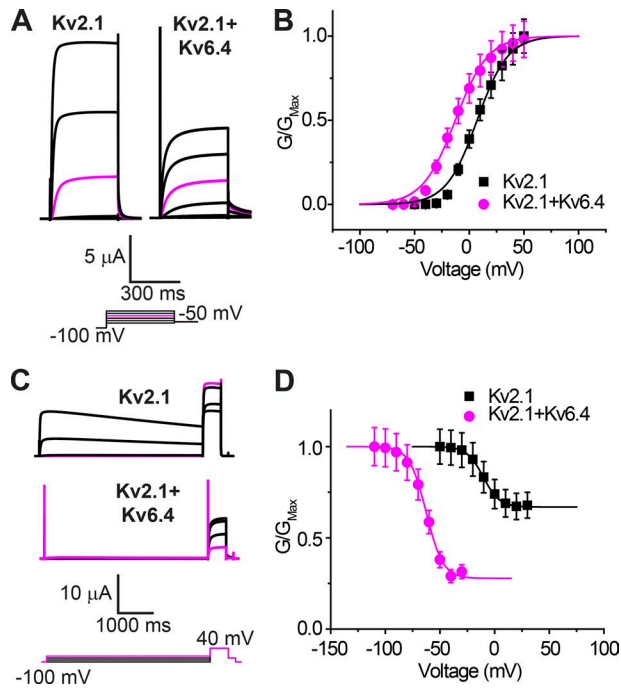
Figure 3. **Comparison of gating properties of Kv2.1 homomers and Kv2.1:Kv6.4 heteromers. (A)** Example currents recorded under TEVC from oocytes expressing Kv2.1 (left) or Kv2.1:Kv6.4 (right) in response to 400-ms depolarizations ranging from –60 to +40 mV in 20-mV increments from a holding potential of –100 mV. Tail currents were recorded at –50 mV. Scale bars are included for current amplitude and time and the voltage protocol is shown below the currents. The step to 0 mV is highlighted in magenta to emphasize the left-shift in voltage activation in Kv2.1:Kv6.4. For Kv2.1:6.4, a 1:10 cRNA ratio was used for the experiments in this figure to produce a predominantly heteromeric current (Fig. 8). **(B)** Normalized GV relationships determined from isochronal tail currents recorded at –50 mV after 400-ms steps to the indicated voltages are shown for Kv2.1 (black, n = 7) and Kv2.1:Kv6.4 (magenta, n = 10). Data points show mean, error bars indicate standard error, and smooth curves represent a single Boltzmann fit of the data. V_{50} and slope values are given in Table 1. The V_{50} values were significantly different (t test, P < 0.001). **(C)** Example currents recorded from oocytes for Kv2.1 and Kv2.1:Kv6.4 during a protocol used to determine SSI. Oocytes were stepped from a holding potential of –100 mV to voltages ranging from –110 to +30 mV in 10-mV increments for 4 s before a 500-ms step to +40 ms to measure current size. For display purposes, here we show currents recorded in response to prepulses from –40 to +20 mV in 20 mV increments for Kv2.1, and from –100 to –40 mV in 20-mV increments for Kv2.1:Kv6.4. The –40 mV sweep is highlighted in magenta for comparison and represents a voltage at which SSI is virtually absent in Kv2.1 and near maximal in Kv2.1:Kv6.4. Thus, a comparison of currents recorded at +40 mV after prepulses to –100 mV and –40 mV can be used to distinguish homomeric and heteromeric current fractions. Scale bars are given for time and current amplitude, and the voltage protocol is shown below the currents. **(D)** Normalized SSI curves for Kv2.1 (black, n = 7) and Kv2.1:Kv6.4 (magenta, n = 10). Data show mean ± SEM, and curves show a single Boltzmann fit of the data. V_{50} and slope values are given in Table 1. Note SSI is incomplete for both Kv2.1 and Kv2.1:Kv6.4; residual pedestal current fractions as determined by Boltzmann fitting are given in Table 1.

date channels. Fluorescence changes in a larger 15-pixel diameter circle near the chosen spot were used to estimate the background fluorescence in order to correct baseline changes. The number of photobleaching steps was then determined using a published step-finding algorithm (Chen et al., 2014). Only spots that were stationary and had stable baselines were included in the analysis. Analysis of all observed step dwell times indicated the time con-

stant for a GFP bleaching step to occur was ~68 s, so >97% of all bleaching events should be captured in 240-s movies.

Sequence alignments

Sequences were aligned for display using the CLUSTALW algorithm as implemented in MEGA7 (Kumar et al., 2016). Sequence logos displayed in Fig. 2 were generated from alignments using WebLogo (Crooks et al., 2004). Supplemental Table 1 contains sequences and accession numbers for all channels included in the sequence logos, and Supplemental Table 2 contains amino acid frequencies at each gate position for the sequence logos.

Molecular modeling

Structural models were based on published open and closed state computational models of Kv1.2 (Pathak et al., 2007) and included the entire conserved T1–S6 regions of Kv2.1 and Kv6.4. Sequence alignments of Kv2.1 and Kv6.4 to Kv1.2 for structural modeling were generated using MUSCLE, as implemented by Jalview (Waterhouse et al., 2009); a FASTA file of aligned sequences is provided (Supplemental text file). Models were built from the alignments using MODELLER (9v8; Sali and Overington, 1994; Martí-Renom et al., 2000; Eswar et al., 2007). For each target (Kv2.1, Kv6.4 and Kv6.4-PIPIIVN), we generated 30 initial models. MODELLER uses a variety of methods (e.g., Z-DOPE, molpdf, GA341) to assess the models. These scores are associated with the estimated accuracy of the model. For each target-based model set, we selected the top candidate model guided by the molecular PDF score (molpdf), which is the sum of all spatial restraints achieved when transferring structural regions from the template to the target. These candidates also had the lowest Z-DOPE scores of the 30 initial models generated for each template. Assembly and visualization of all the tetrameric models was done in VMD (Humphrey et al., 1996) using visual manipulations and custom-written Tcl scripts. We generated four tetramer arrangements: Kv2.1 homomer, Kv2.1:Kv6.4 (3:1R), Kv2.1:Kv6.4 (2:2R diagonal), and Kv2.1:Kv6.4-PIPIIVN (2:2R diagonal). For the first three models, local structural clashes in the models were removed through 1,000-step energy minimization using the Conjugate Energy algorithm, followed by relaxation using short (1 ps) Molecular Dynamics simulation in vacuo at 300°K, and a 100-step energy minimization. All the optimizations were done using NAMD (Phillips et al., 2005) with a CHARMM36 force field (MacKerell et al., 1998). For the Kv2.1:Kv6.4-PIPIIVN model, the gate of the final Kv2.1 homomer model was placed into the final Kv2.1:Kv6.4 2:2R model, and the model was optimized with a 100-step energy minimization, 1 ps thermal relaxation, and then another 100-step energy minimization again with symmetry restraints. The space accessible for the K+ ion center at the pore gate constriction in the open state models was visualized using "solvent" representation for the probe radius set to 1.8 Å (potassium ion in CHARMM36 force field [1.76375 Å] rounded to the nearest 0.1 A) and all the protein atoms having their Van der Waals radius derived from CHARMM36.

Online supplemental information

Supplemental Table 1 contains sequences and accession numbers for all channels included in the sequence logos. Supplemental

Pisupati et al.
Kv6.4 S6 gate influences K+ channel stoichiometry

Journal of General Physiology
https://doi.org/10.1085/jgp.201812121

1707

Table 1.   **Boltzmann fit parameters for Kv2.1 and Kv2.1:Kv6.4 heteromers**

Channel	Activation (GV)		SSI		
	V_{50}[a]	Slope[b]	V_{50}	Slope	Pedestal[c]
Kv2.1[d]	7.2 ± 1.0	14.1 ± 0.3	−10.5 ± 0.6	7.5 ± 0.4	0.67 ± 0.02
+ Kv6.4 WT[e]	−12.8 ± 1.4	15.1 ± 0.4	−62.6 ± 0.6	7.7 ± 0.2	0.28 ± 0.01
+ Kv6.4-PIPIIV-KV2.1 CT[e]	−16.3 ± 0.5	14.2 ± 0.6	−82.3 ± 1.4	12.2 ± 0.5	0.3 ± 0.01

[a]Midpoint of single Boltzmann fit in mV (mean ± SEM).
[b]Slope of single Boltzmann fit (mean ± SEM).
[c]Non-inactivating pedestal current fraction determined from Boltzmann fit (mean ± SEM).
[d]n = 7.
[e]n = 10.

Table 2 contains amino acid frequencies at each gate position. The supplemental text file is a FASTA file of the Kv2.1 and Kv6.4 alignment used for structural modeling.

Results

The highly conserved S6 activation gate sequence degenerates in regulatory subunits

To determine whether there are sequence signatures that accompany the regulatory subunit phenotype (i.e., inability to form functional homotetramers), we compared the amino acid sequences of eight evolutionarily distinct clusters of regulatory subunits comprising 43 proteins from mouse and sea anemone (*Nematostella vectensis*) that arose independently as determined by phylogenetic analyses (Jegla et al., 2012; Li et al., 2015b). We restricted the analysis to these two species because the phenotype for each regulatory subunit cluster has been experimentally verified. In mammals, the 10 Kv2 subfamily regulatory subunits can be split into two groups with separate evolutionary origins: (1) Kv5.1, which first appeared in chordates, and (2) Kv6–9, which later arose independently in vertebrates (Li et al., 2015b). In *N. vectensis*, six additional evolutionarily independent clusters of regulatory subunits can be found in the Kv1 (four clusters), Kv3 (one cluster), and Kv4 (one cluster) subfamilies (Jegla and Salkoff, 1997; Jegla et al., 2012; Li et al., 2015b). We found no consistent regulatory subunit sequence alterations in the subfamily-specific T1 assembly domain, but 42 of 43 regulatory subunits contained unusual substitutions in the C terminal of S6 (P**V**PVI**V** in *Drosophila* Shaker), a region that is typically among the most highly conserved in Shaker-like Kv channels (Fig. 2, A–C). This sequence includes the proline gating hinge and forms extensive intersubunit contacts in the structure of the mammalian Shaker channel Kv1.2 (Long et al., 2005a). The bold residues, V474 and V478 in *Drosophila* Shaker, face inward toward the conduction pathway, forming a hydrophobic seal in the closed state (Long et al., 2005a). Access to V474 in Shaker is gated by pore opening, while access to V478 is possible in both open and closed channels, suggesting that V478 forms the cytoplasmic boundary of the intracellular activation gate (Liu et al., 1997; del Camino and Yellen, 2001; Hackos et al., 2002; Webster et al., 2004; del Camino et al., 2005). To facilitate comparison of gate sequences between channels, in this paper we will number residues by their posi-

tion within the six-amino acid (PVPVIV) gate sequence; in this nomenclature, V474 is V2 and V478 is V6. Each independent cluster of regulatory subunits has a distinct pattern of substitutions in this activation gate sequence (Fig. 2, D–K), with several types of substitutions occurring multiple times. These include loss or displacement of one of the gating hinge prolines, insertion of polar residues that disrupt gate hydrophobicity, or insertion of large aromatics that could potentially cause steric conflicts. In the mammalian Kv6–9 cluster, P3 is lost (nine of nine proteins) and replaced with a polar residue (S/T, eight of nine proteins), and an aromatic is inserted in place of V6 (eight of nine proteins; N in Kv8.1; Fig. 2 D). Site-directed mutagenesis of Shaker has found that hydrophilic substitutions at P3 can destabilize the closed state (Sukhareva et al., 2003), and aromatic substitution of V6 (V6W) results in nonconducting channels (Hackos et al., 2002).

Since mutations within the Shaker activation gate have been shown to disrupt channel function and expression (Hackos et al., 2002; Kitaguchi et al., 2004), we hypothesized that the unusual substitutions observed in regulatory subunit gate sequences could play a role in restricting the functional stoichiometry of regulatory subunit-containing heteromers. To test this hypothesis, we chose mouse Kv2.1/Kv6.4 heteromers as a model system because analysis of gating current components supports a 3:1R stoichiometry (Bocksteins et al., 2017), and heteromeric channels can be functionally distinguished from Kv2.1 homomers based on gating properties (Fig. 3 and Table 1). In oocytes coexpressing Kv2.1 and Kv6.4, currents arising from Kv2.1:Kv6.4 heteromers can be differentiated from currents arising from Kv2.1 homomers based on closed state inactivation, which is present only in the heteromers (Fig. 3, B–D). Heteromer contributions to currents elicited by a depolarizing test pulse to +40 mV can be selectively eliminated with a prepulse to −40 mV (Fig. 3, C and D), allowing for functional estimates of heteromer:homomer ratios in oocytes expressing both channels.

TIRF microscopy reveals multiple Kv2.1:Kv6.4 heteromer stoichiometries

We used a TIRF microscopy single-molecule bleaching assay to determine the stoichiometry of Kv2.1:Kv6.4 heteromers. TIRF single-molecule bleaching assays have been successfully used to determine the subunit stoichiometry of many different types of ion channels and other membrane-associated proteins (Ulbrich
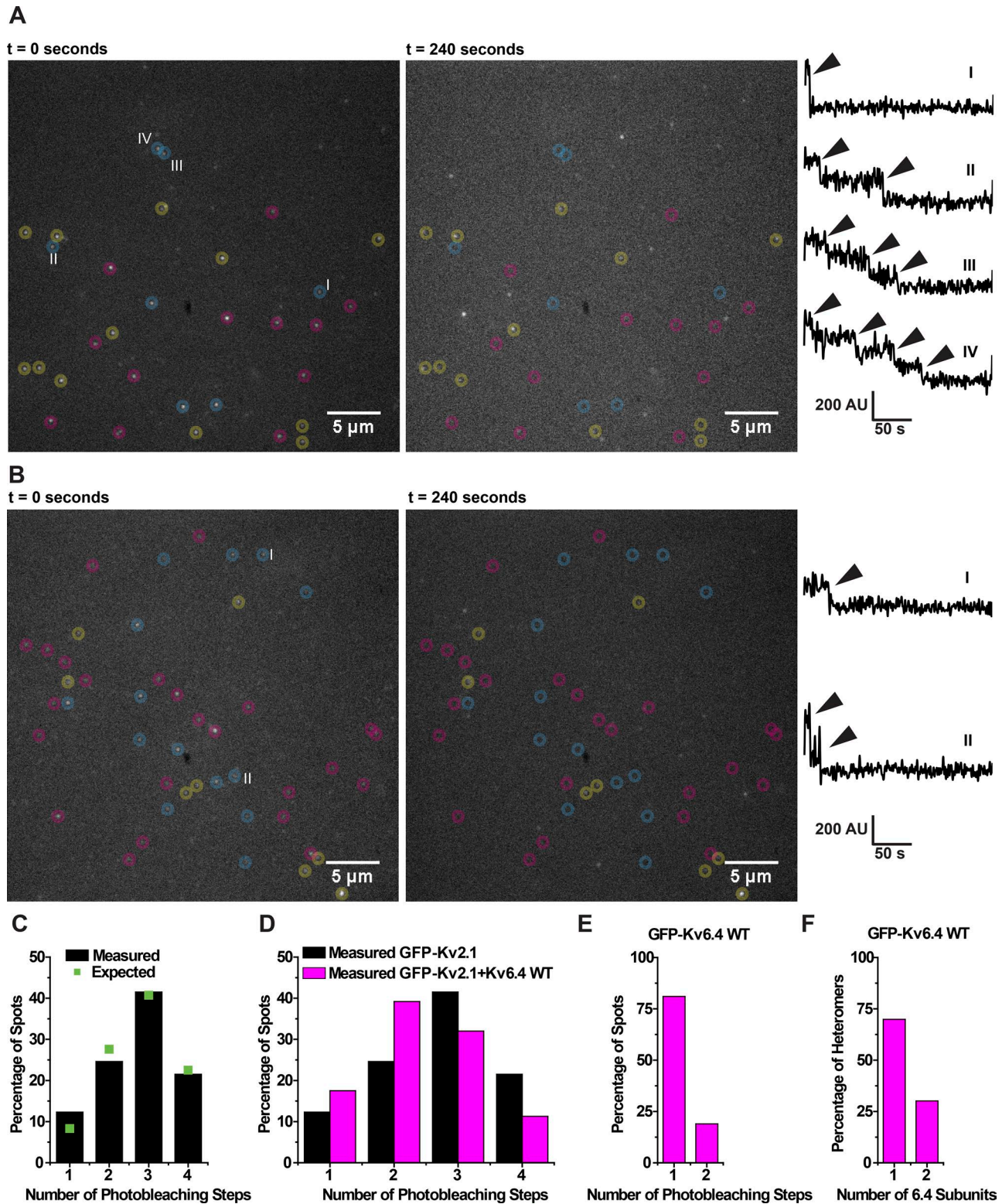
Figure 4. **Determination of Kv2.1:Kv6.4 heteromer stoichiometry by TIRF photobleaching assay. (A)** Example TIRF images from an oocyte expressing GFP-Kv2.1 before (left) and after photobleaching (middle). Spots that bleached to background during the photobleaching period (blue circles) were analyzed for number of bleaching steps. Bleach-resistant spots (yellow circles) or spots that bleached but did not have a stable baseline (magenta) were not included in the analysis. Example fluorescence traces for spots in the movie bleaching in one (I), two (II), three (III) and four (IV) steps are shown at the right margin. Fluorescent spots (circled) bleachable in discrete steps were observed only in oocytes expressing GFP-tagged channels. **(B)** Example TIRF images and fluorescence traces before and after photobleaching for Kv2.1 coexpressed with GFP-Kv6.4, labeled as in A. Only spots with one or two bleaching steps were observed. **(C)** Frequency distribution of bleaching steps for channel spots in oocytes expressing GFP-Kv2.1 (Kv2.1 homomers). Only spots bleaching in one to four steps were observed. Assuming all channels are tetramers with four GFPs, a binomial fit of the distribution (squares) estimates the probability of detecting GFP fluorescence

and Isacoff, 2007; Nakajo et al., 2010; Coste et al., 2012; Upadhyay et al., 2016). We chose this approach because it allows identification and quantification of minor heteromer species that would likely be missed by macroscopic analyses such as intersubunit FRET and gating currents that have previously been used to look at Kv2.1:Kv9.3 and Kv2.1:Kv6.4 stoichiometry (Kerschensteiner et al., 2005; Bocksteins et al., 2017). In this technique, individual membrane surface–expressed channels containing fluorescently tagged subunits (visible as fluorescent dots) are bleached with a laser, and the number of bleaching steps is counted to infer fluorescent subunit numbers (see Methods and Ulbrich and Isacoff, 2007).

The N terminus of Shaker-like Kv channels is highly variable even among closely related channels, so we reasoned that N-terminal GFP fusions could be used for TIRF experiments with minimal effect on channel function. When we expressed GFP-Kv2.1 by itself in *Xenopus* oocytes to exclusively form Kv2.1 homotetramers, or Kv2.1 with GFP-Kv6.4 to introduce heteromer formation, we observed fluorescent spots that bleached in discrete steps (Fig. 4, A and B). For GFP-Kv2.1 homomers, fluorescent spots bleached in one, two, three, and four steps (Fig. 4 A). From the distribution of channels bleaching in one to four steps, we estimated the probability for detection of an individual GFP fluorophore to be ~69% (Fig. 4 C). Coexpressing GFP-Kv2.1 with Kv6.4 significantly shifted the distribution toward fewer bleaching steps (P < 0.05, Fisher's exact test), consistent with a reduction in the average number of Kv2.1 channels/subunit through heteromer formation (Fig. 4 D). Note that while the percentage of channels in this Kv2.1:Kv6.4 coexpression experiment bleaching in four steps is significantly reduced, their presence suggests some Kv2.1 homomers are still formed. Residual homomer formation makes it difficult to calculate the stoichiometry of the heteromers with GFP-Kv2.1. Therefore, we coexpressed WT Kv2.1 with GFP-Kv6.4 in a 1:50 ratio to maximize formation of heteromers and to selectively detect heteromers to calculate their stoichiometry. With the GFP tag on Kv6.4 instead of Kv2.1, spots predominantly bleached in one step (consistent with a 3:1R stoichiometry), but to our surprise, there were also a significant number of spots bleaching in two steps (Fig. 4, B and E). Using the GFP bleaching probability determined from the GFP-Kv2.1 experiment (0.69), 2:2R heteromers were estimated to represent ~30% of all heteromers in this experiment (Fig. 4 F). The absence of spots bleaching in three to four steps is consistent with the idea that T1 incompatibility would block assembly of heteromeric channels with more than two Kv6.4 subunits. Coexpressing Kv2.1 with GFP-Kv6.4 in a 15:1 ratio decreases 2:2R significantly to 13% (P < 0.05, χ² test), demonstrating that the proportion of 2:2R heteromers formed depends on the Kv2.1:GFP-Kv6.4 ratio and is therefore not an artifact of the bleaching

step counting procedure. These results provide evidence that Kv2.1:Kv6.4 2:2R heteromers can form but also suggest that their formation is highly inefficient compared with 3:1R heteromers. If the two stoichiometries formed with equal probability, we would expect 2:2R heteromers to predominate at the 1:50 RNA ratio of Kv2.1:GFP-Kv6.4.

The S6 gate of Kv6.4 limits formation of 2:2R heteromers

We next examined the role of the Kv6.4 T1 domain and the Kv6.4 S6 activation gate in restricting the formation of 2:2R heteromers. In keeping with our prediction that T1 self-incompatibility should not be sufficient to block formation of 2:2R heteromers (Fig. 1), coexpressing Kv2.1 with a Kv6.4 chimera containing the self-compatible T1 of Kv2.1 (GFP-Kv6.4-Kv2.1T1; Fig. 5 A) did not significantly increase the formation of 2:2R heteromers as measured by TIRF (Fig. 5 B). However, when Kv2.1 was coexpressed with a Kv6.4 chimera containing the Kv2.1 S6 activation gate (PIPIIV) and C terminus (Kv6.4-PIPIIV-Kv2.1CT; Fig. 5 A), 2:2R heteromer formation was significantly increased to ~60% (Fig. 5 B; P < 0.01, χ² test). This represents an approximately fourfold increase in the efficiency of 2:2R formation relative to 3:1R formation, because it increases the 2:2R abundance from roughly 0.4 times to 1.5 times the 3:1R abundance. 2:2R formation with the GFP-Kv6.4-PIPIIV-Kv2.1CT chimera was concentration dependent and higher than 2:2R formation with WT Kv6.4 over a broad concentration range (Fig. 5 C). We included the Kv2.1 C terminus in this original gate chimera because the C terminus of Kv2.1 has previously been implicated in channel assembly (Mohapatra et al., 2008). A Kv6.4 chimera that retains the Kv6.4 activation gate (PATSIF) and includes only the Kv2.1 C terminus (GFP-Kv6.4-Kv2.1CT; Fig. 5 A) did not increase 2:2R formation (Fig. 5 D), specifically implicating the activation gate as the key region for increasing 2:2R formation within the Kv6.4-PIPIIV-Kv2.1CT chimera. Furthermore, the chimera Kv6.4-PIPIIV, which contains only the Kv2.1 activation gate, was also able to increase 2:2R formation (Fig. 5 D). Adding the Kv2.1 T1 to the Kv6.4-PIPIIV-Kv2.1CT (Kv6.4-Kv2.1T1-PIPIIV-Kv2.1CT) did not further increase 2:2R formation (Fig. 5 D) and did not form homotetramers as measured by TIRF (see Fig. 5 legend for step counts) or outward current recorded at +40 mV (143 ± 14 nA, n = 3). This is consistent with previous observations that the substitution of the Kv6.4 T1 and S6 with Kv2.1 sequences is not sufficient to confer homotetramer formation to Kv6.4 (Ottschytsch et al., 2005). The Kv6.4-Kv2.1T1-PIPIIV-Kv2.1CT chimera supports our hypothesis that the self-incompatible Kv6.4 T1 is not responsible for preferential assembly of Kv2.1:Kv6.4 3:1R heteromers over 2:2R heteromers, but also suggests that T1 is not entirely responsible for Kv6.4 subunit self-incompatibility.

We next investigated the role of the two most unusual residues of the Kv6.4 activation gate (T3 and F6; Fig. 2) in reducing 2:2R

and bleaching at 69% in our experimental setup. **(D)** Frequency distribution of bleaching steps for channel spots in oocytes coexpressing GFP-Kv2.1 and Kv6.4 compared with GFP-Kv2.1 alone. The addition of Kv6.4 RNA significantly reduces the frequency of four steps from 22% to 11% and reduces the frequency of three steps from 42% to 32%. There is a corresponding increase in the frequency of two steps from 25% to 39% and an increase in the frequency of one steps from 12% to 17% (P < 0.05, Fisher's exact test). This shift in step distribution confirms detection of Kv2.1:Kv6.4 heteromer formation. **(E)** Frequency distribution of bleaching steps for channel spots in oocytes injected with Kv2.1:GFP-Kv6.4 in an ~1:50 ratio to maximize heteromer formation. Only spots bleaching in one to two steps were observed, and 81% bleach in one step. **(F)** Relative frequency of 3:1R and 2:2R Kv2.1:GFP-Kv6.4 heteromers calculated from the bleaching step distribution using the 69% GFP detection probability determined for Kv2.1 homomers as described in C..
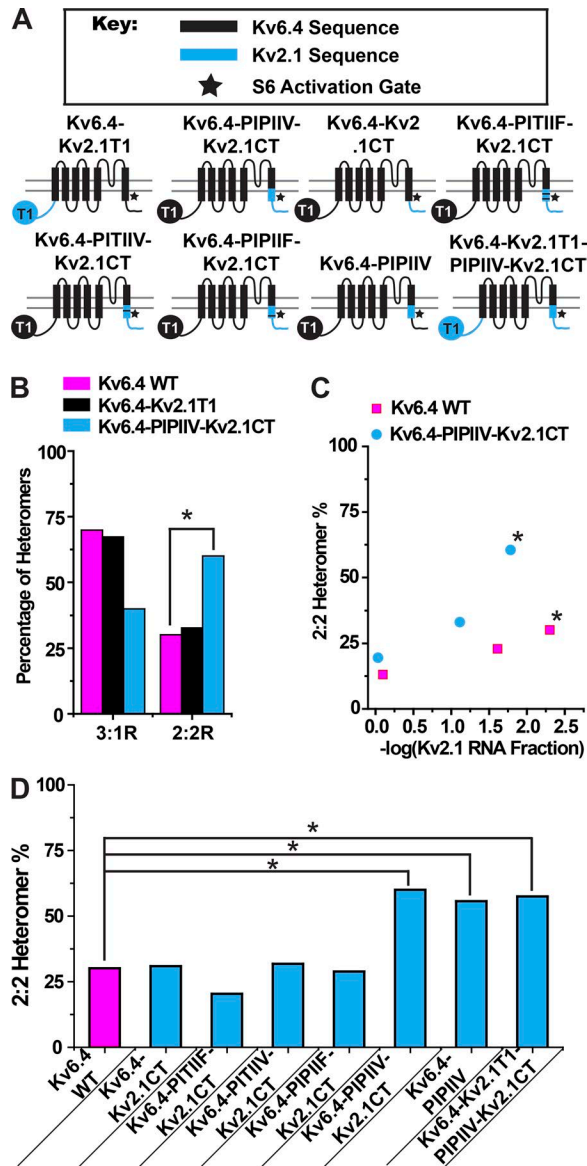
Figure 5. **The Kv6.4 activation gate but not T1 limits the formation of Kv2.1:Kv6.4 2:2R heteromers. (A)** Schematic diagram of the chimeric constructs used to test 2:2R formation by TIRF microscopy. The N-terminal T1 domain is labeled, and transmembrane domains S1–S6 are shown as rectangles, with a star next to the S6 activation gate. Sequences derived from Kv6.4 are shown in black, and sequences inserted from Kv2.1 are shown in blue. Chimera names are given below each diagram. **(B)** Percentages of 3:1R and 2:2R heteromers calculated from TIRF photobleaching assays for Kv2.1 coexpressed with GFP-tagged versions of WT Kv6.4 (magenta), Kv6.4-Kv2.1T1 (black), and Kv6.4-PIPIIV-Kv2.1CT (blue). The stoichiometry distribution for Kv6.4-Kv2.1T1 was unchanged, but Kv6.4-PIPIIV-Kv2.1CT had significantly fewer 3:1R heteromers and significantly more 2:2R heteromers ($P < 0.05$, χ^2 test). Kv2.1 was expressed with Kv6.4-Kv2.1T1 and Kv6.4-PIPIIV-Kv2.1CT in a 1:80 and a 1:60 cRNA ratio, respectively, to eliminate Kv2.1 homomers and bias 2:2R heteromer formation. **(C)** Expression ratio dependence of 2:2R heteromer formation is shown for WT Kv6.4 and Kv6.4-PIPIIV-Kv2.1CT. 2:2R formation was significantly higher for both constructs at the highest concentration tested relative to lower concentrations (*, $P < 0.05$, χ^2 test). Note 2:2R formation is higher for Kv6.4-PIPIIV-Kv2.1CT across a broad range of expression ratios. **(D)** Kv2.1:Kv6.4 2:2R heteromer percentages detected for all Kv6.4 chimeras tested in TIRF photobleaching assays at a highly Kv6.4-biased expression ratio. 2:2R formation was significantly increased relative to WT for the Kv6.4-PIPIIV-Kv2.1CT, Kv6.4-PIPIIV, and Kv6.4-Kv2.1T1-PIPIIV-Kv2.1CT

formation by introducing them back into the GFP-Kv6.4-PIPIIV-Kv2.1CT chimera. We chose this chimera instead of GFP-Kv6.4-PIPIIV because it displayed the highest 2:2R formation. When T3 and F6 were reintroduced into Kv6.4-PIPIIV-Kv2.1CT together or individually (Fig. 5 A), the proportion of 2:2R heteromers was statistically identical to the 2:2R proportion we observed for WT Kv6.4 (Fig. 5 D). These results as a whole show that the unusual T3 and F6 substitutions in the Kv6.4 S6 activation gate, and not T1 incompatibility, play a significant role in suppressing Kv2.1:Kv6.4 2:2R heteromer formation.

The Kv6.4 gate limits functional contributions of 2:2R heteromers

While our TIRF results suggest that 2:2R Kv2.1-Kv6.4 heteromers do form at a low rate, and that the efficiency of formation is increased by substitution of Kv2.1 gate residues into Kv6.4, they do not address the question of whether 2:2R heteromers incorporating either WT Kv6.4 or Kv6.4-PIPIIV-Kv2.1CT contribute significantly to macroscopic currents. To examine 2:2R current contributions, we first verified that currents generated by Kv2.1:Kv6.4-PIPIIV-Kv2.1CT heteromers, like currents from Kv2.1:Kv6.4 WT heteromers, can be distinguished from Kv2.1 homomer currents based on SSI (Fig. 6 and Table 1). In oocytes expressing a 1:10 ratio of Kv2.1:Kv6.4-PIPIIV-Kv2.1CT, the V_{50} of steady-state we measured was -82.32 ± 1.43 mV, compared with -62.56 ± 0.58 mV for oocytes expressing Kv2.1:Kv6.4 WT. Thus a -40 mV prepulse can also be used to distinguish the current fraction contributed by Kv2.1:Kv6.4-PIPIIV-Kv2.1CT heteromers from the Kv2.1 homomer current fraction. We do not think it is safe to attribute the increased hyperpolarized shift in SSI to the presence of functional 2:2R channels, because the altered S6 gate of Kv6.4-PIPIIV-Kv2.1CT could also directly impact the gating of 3:1R heteromers in unpredictable ways. We did not observe obvious changes in SSI properties based on the Kv2.1:Kv6.4-PIPIIV-Kv2.1CT and therefore did not examine SSI in detail for signs of multiple functionally distinct heteromeric species.

We instead measured total current size and calculated heteromer current size in oocytes injected with a constant amount of Kv2.1 cRNA titrated against increasing amounts of either Kv6.4 or Kv6.4-PIPIIV-Kv2.1CT cRNA to gain insights into the functionality of 2:2R heteromers. Assuming that tetrameric channels form as a dimer of dimers, as has been previously suggested (Tu and Deutsch, 1999), the availability of Kv2.1 homodimers required for 3:1R formation should drop as the expression of Kv6.4 increases and favors heterodimer formation. Therefore, the absolute number of 3:1R channels that can be formed should drop and become extremely small at highly Kv6.4-biased expression ratios.

constructs (*, $P < 0.05$, χ^2 test). The P3T and V6F mutations in the Kv6.4-PIPIIV-Kv2.1CT background eliminate the increase in 2:2R formation. Bleaching step counts and expression ratios for the data in D were as follows (construct name, ratio, no. of one-steps, no. of two-steps): Kv6.4 WT, 1:200, 98, 23; Kv6.4-Kv2.1CT, 1:142, 87, 21; Kv6.4-PITIIF-Kv2.1CT, 1:154, 85, 13; Kv6.4-PITIIV-Kv2.1CT, 1:128, 64, 16; Kv6.4-PIPIIF-Kv2.1CT, 1:334, 67, 15; Kv6.4-PIPIIV-Kv2.1CT, 1:60, 72, 39; Kv6.4-PIPIIV, 1:185, 80, 39; and Kv6.4-Kv2.1T1-PIPIIV-Kv2.1CT, 1:78, 63, 32. We did not detect spots bleaching in three or four steps for any GFP-Kv6.4 chimera tested in this study.
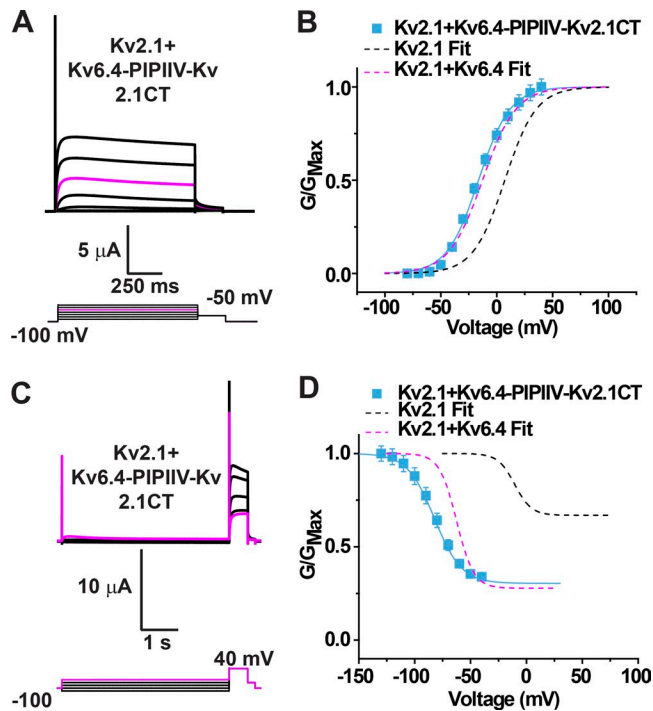
Figure 6. **Biophysical properties of heteromeric currents from oocytes coexpressing Kv2.1:Kv6.4-PIPIIV-Kv2.1CT. (A)** Example currents recorded from an oocyte expressing Kv2.1:Kv6.4-PIPIIV-Kv2.1CT in a 1:10 ratio in response to 1-s voltage steps ranging from –80 to +40 mV in 20-mV increments from a holding potential of –100 mV. The voltage protocol is shown below the currents, the 0-mV trace is highlighted in magenta, and scale bars are given for time and current amplitude. **(B)** Normalized GV relationship for Kv2.1+Kv6.4-PIPIIV-Kv2.1CT determined from isochronal tail currents recorded at –50 mV after 1-s steps to the indicated voltages. Data points show mean ± SEM (n = 10), and the solid blue curve represents a single Boltzmann distribution fit of the data (V_{50} and slope are included in Table 1). Dashed magenta and black curves show the Boltzmann fits for Kv2.1 homomers and Kv2.1:Kv6.4 WT, respectively. **(C)** Example current traces for the SSI protocol for an oocyte expressing Kv2.1:Kv6.4-PIPIIV-Kv2.1CT in a 1:10 cRNA ratio. The voltage protocol is indicated below the current, the oocyte was held at –100 mV and current traces recorded in response to 4-s prepulses ranging from –120 to –40 mV in 20-mV increments are shown, and the –40 mV trace is highlighted in magenta. Pre-pulses were followed by a 500-ms step to +40 mV to show current availability. **(D)** Normalized SSI relationship determined for Kv2.1:Kv6.4-PIPIIV-Kv2.1CT from peak current amplitudes recorded at +40 mV following 4-s prepulses to the indicated voltages. Data show mean ± SEM (n = 10), the blue curve represents a single Boltzmann fit (parameters in Table 1), and the dashed magenta and black curves show Boltzmann fits for Kv2.1 and Kv2.1:Kv6.4 WT, respectively.

If 3:1R channels are the only functional heteromeric species and/or 2:2R formation is highly inefficient, as for Kv2.1:Kv6.4, then current size should approach 0 as the Kv6.4 expression ratio is increased. Fig. 7 A depicts predicted changes in the composition and relative abundance of surface-expressed channels in oocytes expressing Kv2.1 and Kv6.4 at various expression ratios incorporating the efficiency of 2:2R formation we determined in TIRF. In contrast, if both the 3:1R and 2:2R heteromers are functional, and 2:2R formation is more efficient as we observed for Kv2.1:Kv6.4-PIPIIV-Kv2.1CT using TIRF, the current size should drop off less with increasing regulatory subunit expression due to current flowing through the 2:2R heteromers. A prediction for

the composition and relative abundance of surface-expressed channels for Kv2.1:Kv6.4-PIPIIV-Kv2.1CT at various expression ratios using TIRF data on 3:1R/2:2R ratios is shown in Fig. 7 B. Based on these predictions, we reasoned it would be possible to tell whether Kv2.1:Kv6.4-PIPIIV-Kv2.1CT 2:2R heteromers are functional if current is significantly increased relative to Kv2.1:Kv6.4 in oocytes injected with high concentrations of the Kv6.4 species relative to Kv2.1. It would be difficult to make conclusions regarding 2:2R functionality for Kv2.1:Kv6.4 from an expression ratio titration alone, because the absolute number of 2:2R channels is predicted to be very small, and thus current might approach 0 at high Kv6.4 concentrations regardless of 2:2R functionality (Fig. 7 A).

A comparison of current sizes for experimental titrations of WT Kv6.4 and Kv6.4-PIPIIV-Kv2.1CT cRNA against a constant amount of Kv2.1 cRNA is shown in Fig. 8, A and B. During electrophysiological recordings, oocytes were held at –100 mV for 500 ms, followed by a 4-s hyperpolarizing prepulse to –120 mV to relieve closed state inactivation, and then pulsed to +40 mV for 500 ms to measure current size. With Kv6.4, total current elicited by a +40 mV depolarization dropped rapidly as Kv6.4 cRNA levels were increased and approached 0 at a Kv6.4:Kv2.1 100:1 ratio (Fig. 8 C). Current levels also decreased with increasing Kv6.4-PIPIIV-Kv2.1CT titration but were significantly higher across almost the entire titration, with 43 ± 3.7% of the control current level remaining at a 1:50 ratio of Kv2.1:Kv6.4-PIPIIV-Kv2.1CT, the highest expression level we tested (Fig. 8 C). cRNA ratios differed slightly between the two titrations, so we statistically compared means from the closest cRNA ratios (Fig. 8 C, brackets). The current size in the Kv2.1:Kv6.4-PIPIIV-Kv2.1CT titration compared with the Kv2.1:Kv6.4 titration increased from 1.06 ± 0.22-fold (mean ± SD) at low expression ratios to 4.22 ± 0.60-fold (mean ± SD) at high ratios (Fig. 8 D), suggesting that 2:2R heteromers that should become more abundant at high ratios are significantly contributing to currents in the Kv2.1:Kv6.4-PIPIIV-Kv2.1CT titration.

We do not think that differences in single-channel conductance Kv2.1:Kv6.4 and Kv2.1:Kv6.4-PIPIIV-Kv2.1CT 3:1R heteromers could explain the differences in the titrations. We compared single-channel conductance for Kv2.1 homomers and Kv2.1:Kv6.4 heteromers expressed in *Xenopus* oocytes using on-cell patches. We observed channels with a conductance of 8.3 ± 0.7 pS in oocytes expressing only Kv2.1 (Fig. 8, E and G). In oocytes expressing Kv2.1 and Kv6.4, we observed channels with conductance statistically identical to these Kv2.1 homomers and one additional group of channels with an approximately one-third smaller conductance, which presumably represent Kv2.1:Kv6.4 heteromers (Fig. 8, F and G). This small single-channel conductance drop would predict some dropoff in current at points in the titration where 3:1Rs are predicted to be abundant, but it is not sufficient to explain the near complete loss of current at high Kv6.4 cRNA concentrations. The latter current loss likely corresponds to the expected reduction in 3:1R formation at high Kv6.4 concentrations that is not compensated by current flowing through 2:2R heteromers because of their low abundance and/or reduced functionality. If the difference we observed in whole cell current size in the Kv2.1:Kv6.4 and Kv2.1:Kv6.4-PIPIIV-Kv2.1CT titrations at highly Kv6.4-biased ex-
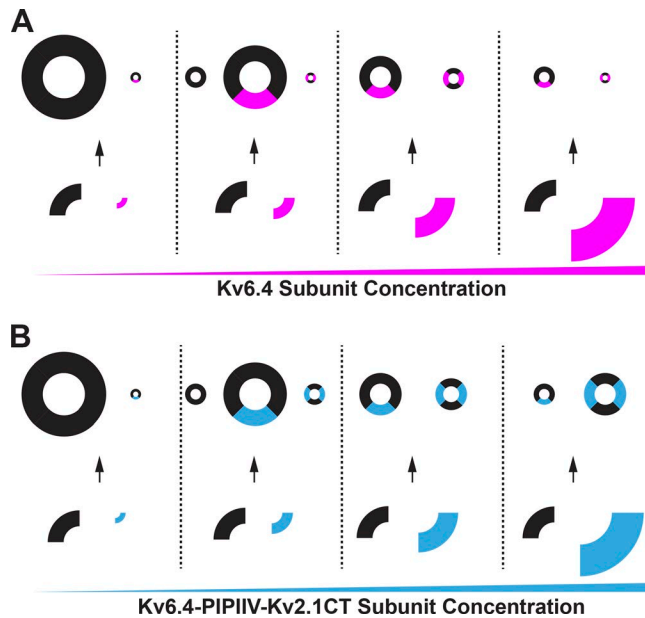
Pisupati et al.
Kv6.4 S6 gate influences K⁺ channel stoichiometry

Journal of General Physiology
https://doi.org/10.1085/jgp.201812121

1712

Figure 7. **Predicted stoichiometry and abundance of surface-expressed channels for Kv2.1:Kv6.4 and Kv6.4-PIPIIV-Kv2.1CT at various expression ratios.** Surface-expressed channel tetramers are depicted as open circles and colored-in quarters according to subunit composition (Kv2.1, black; Kv6.4, magenta; Kv6.4-PIPIIV-Kv2.1CT, blue). Monomer abundance is shown below the channels; Kv2.1 abundance remains constant while Kv6.4 abundance is increased from left to right. Relative abundance for each stoichiometry of surface-expressed channel and each type of monomer is represented by the size of the respective icon. **(A)** For Kv2.1:Kv6.4, the number of 3:1R heteromers initially increases as Kv6.4 expression is increased, but then drops as availability of Kv2.1 homodimers, which are required for 3:1R formation, becomes limiting at the highest Kv6.4 expression levels. TIRF results show that 2:2R formation is inefficient and never exceeds 30% of the total heteromer population, even at the highest Kv6.4 expression levels. Therefore, the total number of surface-expressed channels will reduce and become very small as Kv6.4 expression is increased against a constant level of Kv2.1 expression. **(B)** For Kv2.1:Kv6.4-PIPIIV-Kv2.1CT, channel abundance is predicted to decrease less precipitously as Kv6.4-PIPIIV-Kv2.1CT expression level increases because 2:2R formation is more efficient, reaching ~60% of all heteromers at the most Kv6.4-PIPIIV-Kv2.1CT–biased expression ratios. Assuming similar levels of 3:1R formation, this represents an approximately fourfold increase in the number of 2:2R heteromers formed compared with Kv6.4.

pression ratios simply reflected a difference in single-channel conductance between 3:1R heteromers, then we would expect that the fold difference in current size across the two titration curves to remain constant, unlike the approximately fourfold change we observed across the titration (Fig. 8 D). We did not pursue single-channel analysis for Kv2.1:Kv6.4-PIPIIV-Kv2.1CT because we reasoned that the introduced gate changes might lessen differences in single-channel conductance, making it difficult to detect multiple heteromer species and unsafe to assign observed conductances to specific stoichiometries. While significant current remains at high concentrations of Kv6.4-PIPIIV-Kv2.1CT cRNA, the current level does diminish >50%. This dropoff could be due to remaining inefficiencies in 2:2R formation (we observed a maximum of ~60% 2:2R heteromers in TIRF) and/or a modest reduction in the single-channel conductance of the 2:2R heteromers relative to 3:1R heteromers and Kv2.1 homomers.

The titration results might also be explained if Kv6.4 WT was translated far more efficiently than Kv6.4-PIPIIV-Kv2.1CT, offsetting the current size reduction in the Kv2.1:Kv6.4-PIPIIV-Kv2.1CT titration. However, we would expect such an offset would also offset the cRNA expression ratio required to achieve a given percentage of heteromeric current. We therefore estimated the contribution of heteromeric current to the total current measured at each point in the titrations using a prepulse to –40 mV to selectively inactivate heteromers. Because SSI of Kv2.1:Kv6.4 heteromers is incomplete, it leaves a pedestal current of a predicted size (Fig. 3 D, Fig. 6 D, and Table 1). We therefore calculated the size of the heteromeric current as the size of the current removed by the –40 mV prepulse plus the predicted size of the corresponding pedestal. Thus, the heteromeric current amplitude was calculated as 1.38 times and 1.44 times the size of the current inactivated by the –40 prepulse for Kv6.4 WT and Kv6.4-PIPIIV-Kv2.1CT, respectively. Plots of total current versus calculated heteromeric current (normalized to the homomeric Kv2.1 controls) are shown for the Kv6.4 WT and Kv6.4-PIPIIV-Kv2.1CT titrations in Fig. 8, H and I. Both titrations approach 100% heteromeric current at a 1:10 Kv2.1:Kv6.4 cRNA ratio, suggesting that there was no significant offset in protein subunit translation that could explain the differences between current size in the titrations. Therefore, we favor differences in of the efficiency of 2:2R formation, and possibly also in 2:2R conduction, as the most likely explanations for the differences between current size in the two expression titrations.

Reduced Cd²⁺ block of Kv2.1 I383C:Kv6.4-PIPIIV-Kv2.1CT heteromers supports 2:2R function

While the cRNA titration experiments shown in Fig. 8 suggest Kv2.1:Kv6.4-PIPIIV-Kv2.1CT 2:2R heteromers conduct and significantly contribute to macroscopic currents, the evidence is indirect. Furthermore, the data are not conclusive for determining whether Kv2.1:Kv6.4 2:2R heteromers are functional. To test functionality of the 2:2R heteromers in a more direct manner, we took advantage of the phenomenon of Cd²⁺ coordination in a Kv2.1 pore cysteine mutant. Rat Kv2.1 I379C is blocked by external cadmium, and block requires coordination by two I379C residues (Krovetz et al., 1997). Furthermore, rat Kv2.1 WT:Kv2.1 I379C heteromers are blocked by Cd²⁺ only if the two cysteines are present in two adjacent subunits; diagonally opposed cysteines do not support cadmium block (Krovetz et al., 1997). We hypothesized that if this mutant (I383C in mouse Kv2.1) was coexpressed with Kv6.4, 3:1R heteromers, which would have adjacent Kv2.1 I383C subunits, should be Cd²⁺-sensitive, while 2:2R heteromers, which would have only diagonally opposed Kv2.1 I383C subunits, would be Cd²⁺-resistant (Fig. 9 A). If 2:2R heteromers contribute to the heteromeric current, then we would expect less cadmium block as the Kv6.4 expression ratio increases. We therefore tested Cd²⁺-sensitivity of Kv2.1 I383C:Kv6.4 WT and Kv2.1 I383C:Kv6.4-PIPIIV-Kv2.1CT at multiple expression ratios to look for evidence of functional 2:2R heteromers.

Kv2.1, Kv2.1:Kv6.4 WT (1:10), and Kv2.1:Kv6.4-PIPIIV-Kv2.1CT (1:10) were all blocked <15% by 500 µM Cd²⁺ (Fig. 9, B and C) compared with >75% block observed for Kv2.1 I383C (Fig. 9 D). While Cd²⁺ block of the WT heteromers was significantly greater
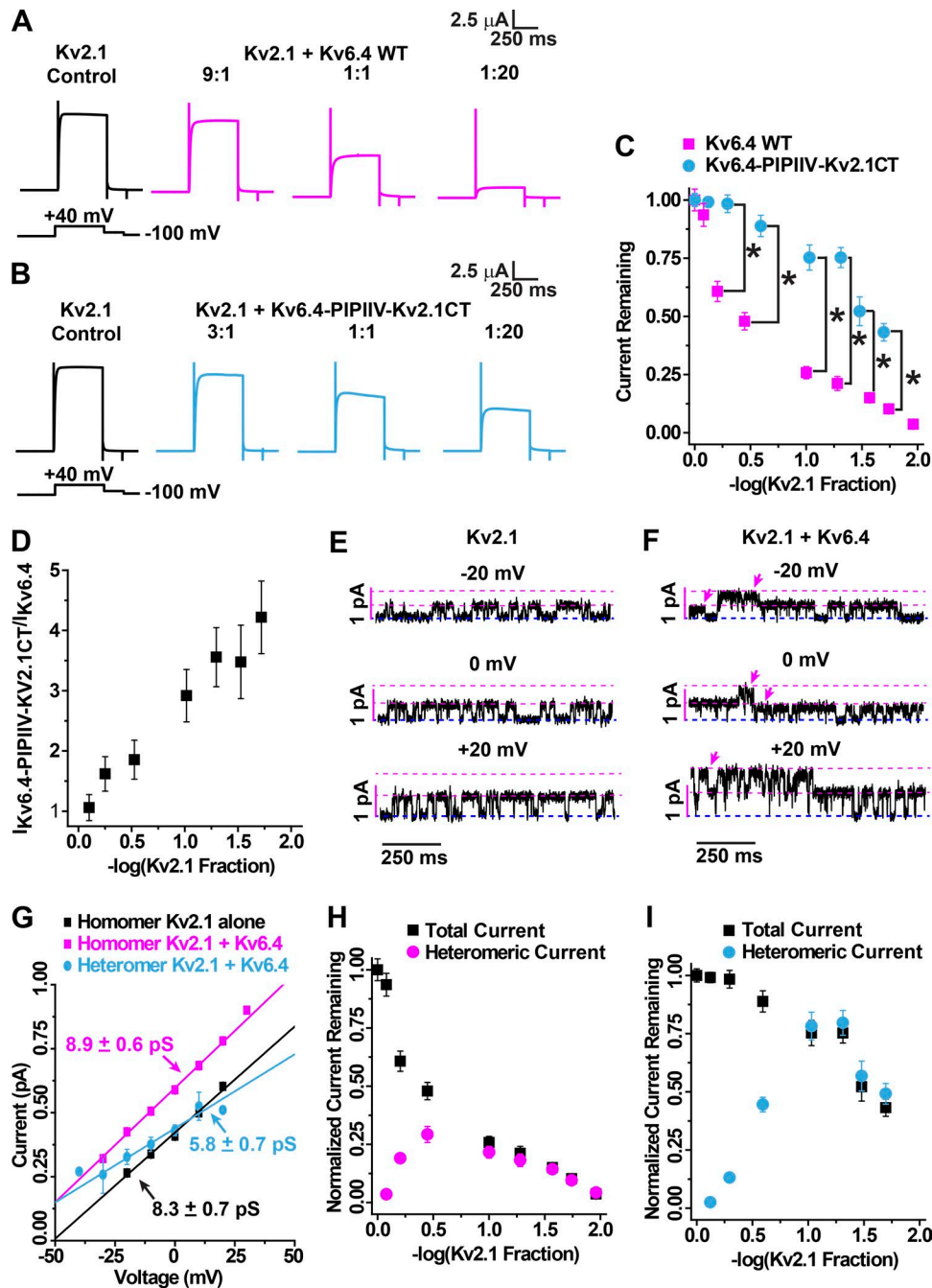
Figure 8. **Kv2.1:Kv6.4 expression ratio titrations predict that 2:2R heteromers have negligible conductance for Kv6.4 WT and are conducting for Kv6.4PIPIIV-Kv2.1CT. (A)** Example currents from oocytes expressing Kv2.1 alone (left, black) or Kv2.1:Kv6.4 WT (magenta) at 9:1, 1:1, and 1:20 ratios. Kv2.1 cRNA level was kept constant, and currents were recorded at +40 mV following a 4-s prepulse to –120 mV to relieve SSI. Note the dramatic decrease in current size as Kv6.4 cRNA level is increased. Scale bars indicate current amplitude and time. **(B)** Example currents from a similar titration of Kv2.1 versus Kv6.4-PIP IIV-KV2.1CT; Kv2.1 control is shown in black, and cRNA ratios shown are 3:1, 1:1, and 1:20. More current is readily apparent at the 1:20 ratio for Kv6.4-PIPIIV-KV2.1CT than Kv6.4 WT. **(C)** Current amplitude versus expression ratio titrations are shown for Kv2.1:Kv6.4 WT (magenta) and Kv2.1:Kv6.4-PIPIIV-KV2.1CT (blue). Expression ratio is given as –log(Kv2.1fraction); 1.0 = a 1:10 Kv2.1:Kv6.4 cRNA ratio. The Kv2.1 cRNA amount remained constant while the Kv6.4 cRNA species amount was varied to achieve the given expression ratio. Data were normalized to the amplitude of control Kv2.1 homomeric currents. Data points show mean ± SEM (n = 10–18 eggs per ratio), and asterisks indicate a significant difference (P < 0.05, t test) between the indicated pairs of data points. **(D)** Normalized current size ratio for Kv2.1:Kv6.4-PIPIIV-KV2.1CT versus Kv2.1:Kv6.4 WT increases approximately fourfold as the Kv6.4 species cRNA is increased. Data show mean ± SD and are derived from the data point pairs statistically compared in C. Kv2.1:Kv6.4 ratios were similar but not identical between the titra-tions, and data are plotted using the average of the Kv2.1:Kv6.4 ratio of the data pair. SD for the ratios was calculated by propagation of error from the original measurements in C. **(E)** Example single-channel current traces from an on-cell patch from an oocyte expressing Kv2.1 alone. Traces were recorded at –20 mV, 0 mV, and +20 mV; the dashed blue line indicates the average closed baseline, and the dashed magenta lines indicate 1× and 2× the average open-channel amplitude for the trace. **(F)** Traces labeled as in D for an on-cell patch containing two channels from an oocyte coexpressing Kv2.1 with Kv6.4. In this example, the dashed magenta lines indicate 1× and 2× the average open-channel amplitude of the largest channel recorded in the trace. Arrows point to examples of

than Kv2.1 homomers, the degree of block was small compared with Kv2.1 I383C and thus does not interfere with detection of enhanced block in channels containing adjacent Kv2.1 I383C subunits. 200 µM DTT increased Kv2.1 I383C current size by 17.9 ± 2.2% (n = 9, P < 0.05, t test), suggesting that partial basal oxidation may interfere with conduction. Therefore, we included 200 µM DTT in all experiments to remove basal oxidation as a potential confounding factor for comparisons of Cd^{2+}-sensitivity. We then examined 500 µM Cd^{2+} block of Kv2.1 I383C:Kv6.4 WT heteromers at varying expression ratios (Fig. 9, D and E). Cd^{2+} significantly slowed the activation of heteromeric channels, but we did not explore the mechanism. We increased test pulse duration to allow currents to reach steady-state for current amplitude measurements. Kv2.1 I383C:Kv6.4 heteromers were blocked to a similar extent as Kv2.1 I383C homomers (~75%), and the degree of block was insensitive to Kv2.1 I383C:Kv6.4 WT expression ratio. In contrast, Cd^{2+}-block in Kv2.1 I383C:Kv6.4-PIP IIV-Kv2.1CT was sensitive to the expression ratio (Fig. 9, D and E). Block was similar to Kv2.1 I383C homomers and Kv2.1 I383C:Kv6.4 WT heteromers with lower concentrations of Kv6.4-PIP IIV-Kv2.1CT cRNA, but the current became significantly more resistant to Cd^{2+} at high Kv6.4-PIPIIV-Kv2.1CT cRNA concentrations (Fig. 9 E). Some Cd^{2+} block remained even at the most biased Kv6.4-PIPIIV-Kv2.1CT expression ratios, consistent with our TIRF experiments, which show that ~40% of the channels at these ratios should still be Cd^{2+}-sensitive 3:1R heteromers. Full block by 500 µM Cd^{2+} could be restored by insertion of an equivalent pore cysteine (M422C) into the Kv6.4-PIPIIV-Kv2.1CT chimera (Fig. 9 F), which ensures that all heteromer stoichiometries produced by coexpression with Kv2.1 I383C would have subunits with adjacent cysteines. The results of these Cd^{2+} block experiments provide a strong line of evidence that Kv2.1:Kv6.4-PIPIIV-Kv2.1CT 2:2R heteromers contribute significantly to macroscopic currents. In contrast, Kv2.1:Kv6.4 2:2R heteromers may not contribute significantly to whole cell currents, because at a 1:10 Kv2.1:Kv6.4 ratio (–log [Kv2.1 fraction] = 1), where virtually all the current is expected to flow through heteromers (Fig. 8 H), and ~20% of the heteromers should be 2:2Rs (Fig. 5 C), we saw no increase in Cd^{2+} resistance. However, because the low 2:2R percentage provides only a small dynamic range for detection of Cd^{2+} resistance, it is not possible to differentiate whether Kv2.1:Kv6.4 2:2R heteromers are completely nonfunctional or have a significantly reduced single-channel conductance relative to Kv2.1:Kv6.4 3:1R heteromers.

Discussion

Our results agree with previous work on Kv6.4 and Kv9.3 that suggest the predominant stoichiometry for mammalian Kv2 subfamily regulatory subunit-containing heteromers is 3:1R (Kerschensteiner et al., 2005; Bocksteins et al., 2017). However, our use of a single-molecule technique (TIRF photobleaching) here revealed that 2:2R heteromers are also formed. Because 2:2R heteromers represent less than a third of all heteromers even at expression ratios highly biased in favor of Kv6.4, 2:2R formation appears to be inefficient and would likely not have been detected in previous studies using macroscopic analysis techniques such as FRET (Kerschensteiner et al., 2005) or gating current components (Bocksteins et al., 2017). T1 self-incompatibility is a key feature of Kv2 subfamily regulatory subunits that helps prevent homophilic subunit interactions, and should rule out formation of 4R, 1:3R, and 2:2R tetramers with adjacent regulatory subunits. However, T1 self-incompatibility should not block formation of 2:2R heterotetramers with diagonally opposed regulatory subunits, the major 2:2R species that would be expected to assemble from Kv2.1:Kv6.4 heterodimers (Fig. 1 E). Our results agree with these expectations for the role of T1 self-incompatibility in assembly of Kv2.1:Kv6.4 heteromers: only 3:1R and 2:2R heteromers were detected in TIRF. However, the ratio of these two stoichiometries was unaffected when the self-incompatible Kv6.4 T1 was replaced with the Kv2.1 T1 (Fig. 5, A and D), suggesting that T1 does not play a major role in driving preferential 3:1R assembly for Kv2.1:Kv6.4 and may not be fully responsible for Kv6.4 subunit self-incompatibility.

While we observed formation of 2:2R Kv2.1:Kv6.4 heteromers, our results suggest that only the more prevalent 3:1R stoichiometry contributes significantly to macroscopic heteromeric currents (Figs. 8 and 9). The 2:2Rs are low abundance and may also have an attenuated single-channel conductance. The unusual activation gate of Kv6.4 and its P3T and V6F substitutions play a key role in limiting 2:2R formation and conduction (Figs. 5, 8, and 9). We did not experimentally examine the mechanism through which these mutations restrict stoichiometry, but we made draft homology models of the pore of Kv2.1, Kv2.1:Kv6.4 heteromers (3:1R and 2:2R) and Kv6.4-PIPIIV (2:2R) to try to gain insights. Open models and closed models were based on the Kv1.2 computational models presented by Pathak et al. (2007). The PD (S5–S6) includes numerous signpost residues universally conserved among Kv1.2, Kv2.1, and Kv6.4 that allow for precise structural alignment (Fig. 10 A). Views of the closed conduction pathway

single- or double-channel openings with smaller than expected amplitudes, indicating a second channel with a lower conductance. **(G)** Plots of single-channel current amplitude versus voltage are given for Kv2.1 homomers expressed in isolation and for presumed homomers and heteromers from oocytes expressing Kv2.1 with Kv6.4. Single-channel conductance values shown on the graph were calculated from linear fits; n was 6 for the two Kv2.1 homomer measurements and 5 for the Kv2.1:Kv6.4 heteromers. The Kv2.1:Kv6.4 heteromer conductance was significantly smaller (P < 0.05, t test). Note there is a small offset in reversal potential between the experiments conducted on oocytes expressing Kv2.1 alone versus Kv2.1 + Kv6.4 that alters single-channel amplitude but does not interfere with conductance measurements; these experiments were conducted at different times with distinct solution batches. **(H)** Normalized total current versus heteromeric current for the Kv2.1:Kv6.4 WT coexpression titration shown in C. To determine the amplitude of the heteromeric current, we selectively inactivated heteromers with a 4-s prepulse to –40 mV before measuring current amplitude at +40 mV. The amplitude of the heteromeric current was determined by adjusting the current fraction removed by the –40 mV prepulse by the fractional inactivation determined from SSI analysis (Figure 3 D and Table 1). In this case, the inactivating fraction was multiplied by 1.38 to account for the observation that 27.8% of heteromeric channels are not expected to inactivate during the prepulse. **(I)** Normalized heteromeric versus total current amplitude for Kv2.1:Kv6.4-PIPIIV-Kv2.1CT; heteromeric fraction was calculated as in H except using a multiplication factor of 1.44 to match the 30.4% pedestal observed for Kv2.1:Kv6.4-PIPIIV-Kv2.1CT in SSI analysis. Note in both titrations the current approaches 100% heteromer at a 1:10 Kv2.1:Kv6.4 species expression ratio (–logKv2.1 fraction = 1).
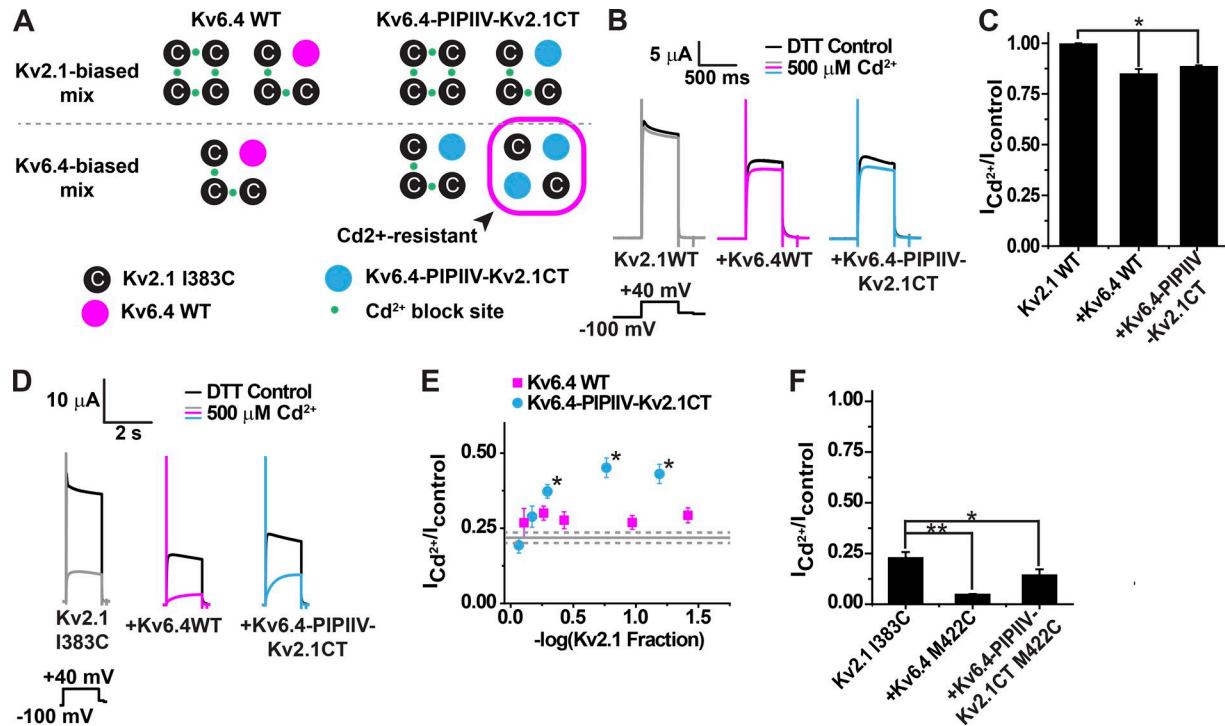
Figure 9. **Cd²⁺ block mediated by adjacent Kv2.1 I383C subunits predicts that 2:2R heteromers contribute to whole cell currents for Kv2.1:Kv6.4-PIP IIV-Kv2.1CT but not for Kv2.1:Kv6.4 WT.** **(A)** Channels predicted to form for Kv2.1 I383C (black circle with C) + Kv6.4 WT (left, magenta) or Kv2.1 I383C + Kv6.4 PIPIIV-Kv2.1CT (right, blue) at Kv2.1-biased or Kv6.4-biased expression ratios. Cd²⁺-coordination sites between adjacent cysteine-containing subunits are marked with green circles; all channels with Cd²⁺-coordination sites are predicted to be sensitive to Cd²⁺ block. Cd²⁺-resistant 2:2R heteromers (magenta box) are predicted to contribute to currents in Kv6.4-PIPIIV-Kv2.1CT-biased mixes. **(B)** Examples current traces before and after addition of 500 µM Cd²⁺ for Kv2.1, Kv2.1:Kv6.4 and Kv2.1:Kv6.4-PIPIIV-Kv2.1CT recorded in response to a 500-ms +40 mV step following a prepulse of 4 s to –100 mV. Oocytes were held at –70 mV. Experiments were performed in the presence of 200 µM dithiotheitol (DTT), and a 1:10 ratio was used for coexpression experiments. Scale bars indicate current amplitude and time. **(C)** Fractional current remaining after 500 µM Cd²⁺ addition determined by measuring the peak current during the +40 mV test pulse using the protocol described in B. Cd²⁺ block was significantly greater of both heteromer species compared with Kv2.1 homomers (*, P < 0.05, ANOVA + Tukey post hoc, n = 10 for each, bars show SEM). **(D)** Examples traces before and after application of 500 µM Cd²⁺ for Kv2.1 I383C, Kv2.1 I383C:Kv6.4 WT, and Kv2.1 I383C:Kv6.4-PIPIIV-Kv2.1CT. Currents were recorded as in B, and a 1:10 Kv2.1:Kv6.4 species expression ratio was used. **(E)** 500 µM Cd²⁺-resistant current fraction (peak current during a 2-s test pulse to +40 mV) is shown for Kv2.1 I383C:Kv6.4 WT (magenta) and Kv2.1 I383C:Kv6.4-PIPIIV-Kv2.1CT (blue) at the indicated cRNA expression ratios. The solid gray and dashed gray lines mark the mean ± SEM of the Cd²⁺-resistant current fraction for Kv2.1I383C homomers. Cd²⁺ block was significantly reduced at high expression ratios for Kv6.4-PIPIIV-Kv2.1CT compared with the lowest expression ratio used (*, P < 0.05, ANOVA, n = 8–11 for each ratio, bars show SEM). **(F)** Kv2.1 I383C homomers (n = 10), Kv2.1 I383C:Kv6.4 M422C heteromers (1:10 ratio, n = 12) and Kv2.1:Kv6.4 M422C-PIP IIV-Kv2.1CT (1:11 ratio, n = 9) heteromers, which are all predicted to have 4 Cd²⁺-coordination sites are highly sensitive to block by 500 µM Cd²⁺ (**, P < 0.01, ANOVA; *, P < 0.05, ANOVA, bars show SEM).

from an extracellular perspective, color-coded by hydrophobicity (Fig. 10, B–E), suggest a feature of the Kv6.4 activation gate that could potentially impact 2:2R heteromer formation. In the Kv2.1 homomer model, the hydrophobic inner gates likely form a vapor lock around the conduction pathway that excludes water from the intersubunit interfaces and allows for strong hydrophobic interactions between subunits (Fig. 10 B). A vapor lock securing a closed state of a channel is a phenomenon common among different unrelated channel families of pro- and eukaryotes, and can be also observed in model hydrophobic pores (Beckstein and Sansom, 2003; Roth et al., 2008; Anishkin et al., 2010). Surface tension of water meniscus above and below the "dry" gate is expected to provide a force contracting the pore walls together, stabilizing the pore assembly. In contrast, a hydrophilic cleft bisects the gate area in Kv2.1:Kv6.4 2:2R heteromers, breaking the vapor lock (Fig. 10 D). With the single Kv6.4 subunit in the 3:1R heteromer, hydrophobicity is locally reduced, but there is no trans-pore hydrophilic cleft (Fig. 10 C). When Kv6.4-PIPIIV

is substituted for WT Kv6.4 in the 2:2R model, the hydrophilic cleft is eliminated, and the vapor lock is restored (Fig. 10 E). This suggests that the hydrophilic cleft in the 2:2R Kv2.1/Kv6.4 heteromers could potentially weaken tetramer stability and may play a role in favoring formation of 3:1R heteromers over 2:2R heteromers even at high Kv6.4 concentrations.

In addition, intracellular views of the pore at the activation gate show that the combination of T3 and F6 of the Kv6.4 gate significantly narrows the conduction pathway in the open state, especially in 2:2R heteromers (Figs. 10, F–M). The opening at the level of F6 in the 2:2R heteromer would require significant dehydration of a K⁺ ion for it to pass, suggesting that conduction for 2:2R heteromers could be energetically unfavorable compared with 3:1R heteromers. The conduction pathway diameter in the 2:2R Kv2.1:Kv6.4-PIPIIV heteromer model, in contrast, has a similar diameter to that of the Kv2.1 homomer model. However, the V6W mutation in Shaker and Kv1.2 does not completely block conduction but instead may energetically trap
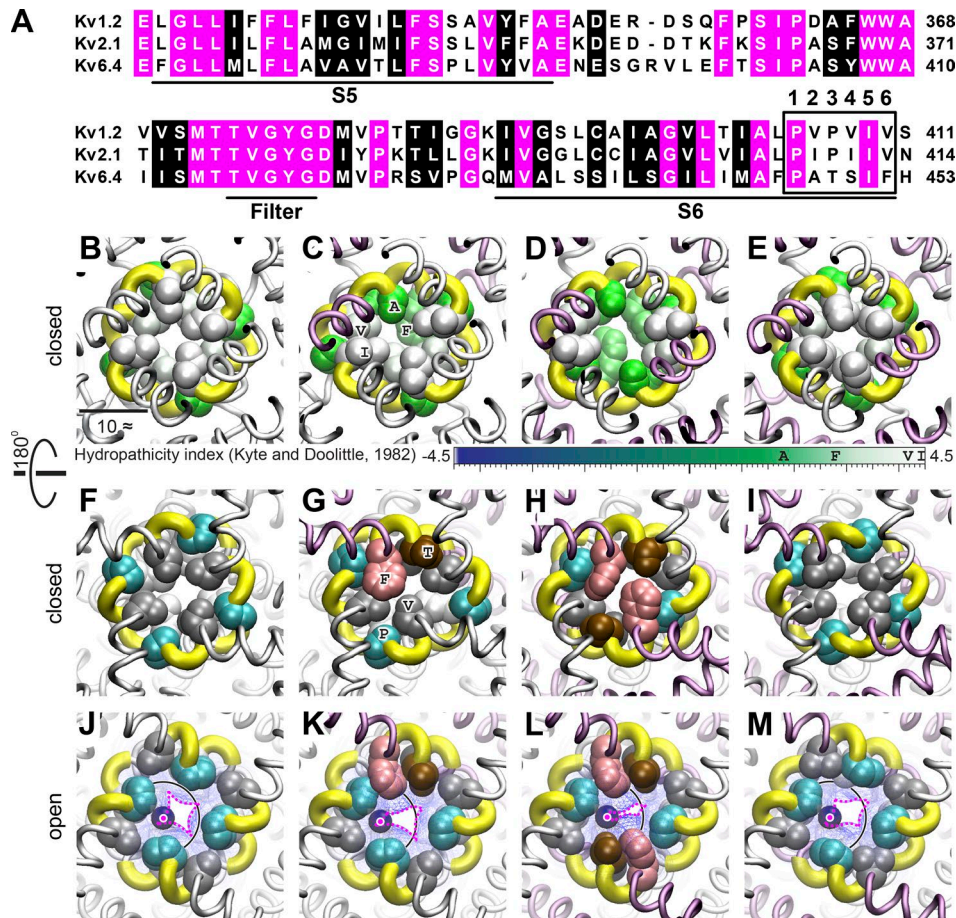
Figure 10. **Structural homology models of Kv2.1 homomers and Kv2.1:6.4 heteromers suggest the Kv6.4 activation gate might perturb pore stability and function.** **(A)** Sequence alignment of the Kv1.2, Kv2.1, and Kv6.4 PDs. Transmembrane domains S5 and S6 and the K⁺ selectivity filter are underlined. Residues identical or conservatively substituted across all three sequences are shaded magenta and black, respectively. The six–amino acid activation gate is boxed with positions 1–6 labeled. Note there are identical signpost residues throughout the PDs allowing precise alignment between Kv1.2 (determined structure, Long et al., 2005a), Kv2.1, and Kv6.4 (structural models based on Kv1.2 presented here). **(B–E)** Snapshots of the closed conduction pathway viewed from the extracellular side for structural models of a Kv2.1 homomer (B), a Kv2.1:Kv6.4 3:1R heteromer (C), a Kv2.1:Kv6.4 2:2R heteromer (D), and a Kv2.1:Kv6.4 2:2R heteromer with the Kv2.1 activation gate (PIPIIV) substituted for the Kv6.4 activation gate (PATSIF; E). The protein backbone (thin tubes) is colored white for Kv2.1 and light purple for Kv6.4. Side chains (van der Waals representation) are shown for positions 2, 3, and 6 of the activation gate and colored according to hydrophobicity index in the Kyte and Doolittle scale with their values ranging from 1.8 for alanine (green) to 4.5 for isoleucine (white; scale provided below panels). Residues that line the conduction pathway (I2 and V6 in Kv2.1; A2 and F6 in Kv6.4) are labeled in C. Yellow ribbons in all panels highlight the position of the gate backbone. In Kv2.1, there is an expected intersubunit hydrophobic vapor lock at the activation gate. While insertion of a single Kv6.4 subunit (C) is well tolerated, insertion of two diagonally opposed Kv6.4 subunits (D) simultaneously introduces a hydrophilic cleft that bisects the gate and increases the distance between diagonally opposed subunits. Both changes favor disruption of the intersubunit vapor lock and could hypothetically reduce tetramer stability at the gate intersubunit interface. **(F–M)** The bottom two rows are the view from the cytoplasmic side—one row for the closed state (F–I) and another for the open (J–M). Side chains at the gate constriction are shown in space fill and colored by the residue type (Kv2.1: I2, white; P3, cyan; V6 gray; Kv6.4: A2, gray; T3, brown; F6, pink). In the closed models, the hydroxyl group of T3 in the Kv6.4 gate faces the neighboring subunit (G and H) and thus contributes to the hydrophilic cleft observed in the extracellular view of the 2:2R tetramer (D). In the open conformations, a dehydrated K⁺ ion (CHARMM36 radius, 1.76 Å) is depicted with a blue circle in the pore opening at the narrowest point of the conduction pathway in the activation gate region. A magenta dashed line surrounds the portion of the opening accessible to the center of the dehydrated K⁺ ion (magenta dot) as determined by rolling the ion against the side chains lining the pore. Blue mesh covers the inaccessible region of the pore. The black circle around the ion roughly approximates the radius of the first hydration shell (i.e., K⁺ radius plus the diameter of the TIP3P water molecule in CHARMM36). While not an explicit simulation in an all-atom setting, it is nevertheless obvious that F6 in the Kv6.4 activation gate narrows the gate opening proportional to the number of Kv6.4 gates. In the 2:2R conformation, almost complete dehydration of a K⁺ ion would be needed for passage. Alternatively, more drastic rearrangements of the backbone than can be observed in our short vacuum simulations might reduce the constriction, but still block conduction by disrupting gating as observed for the F6 substitution in Shaker (Kitaguchi et al., 2004). Note that substitution of the Kv2.1 activation gate into Kv6.4 in the 2:2R simulation restores both the hydrophobic vapor lock of the closed state (E and I) and a wide conduction pathway to the open state (M).

channels in the closed state, propagating structural changes to the selectivity filter that alter gating or conduction (Kitaguchi et al., 2004; Pau et al., 2017). Shaker V6W channels do conduct in a diagonal 2 WT:2 V6W configuration (albeit poorly), and

conduction in homomeric V6W channels can be restored by a compensatory gate mutation P3Q that stabilizes the open state (Sukhareva et al., 2003; Kitaguchi et al., 2004). It should also be noted that because of the ability of individual pore mutations to
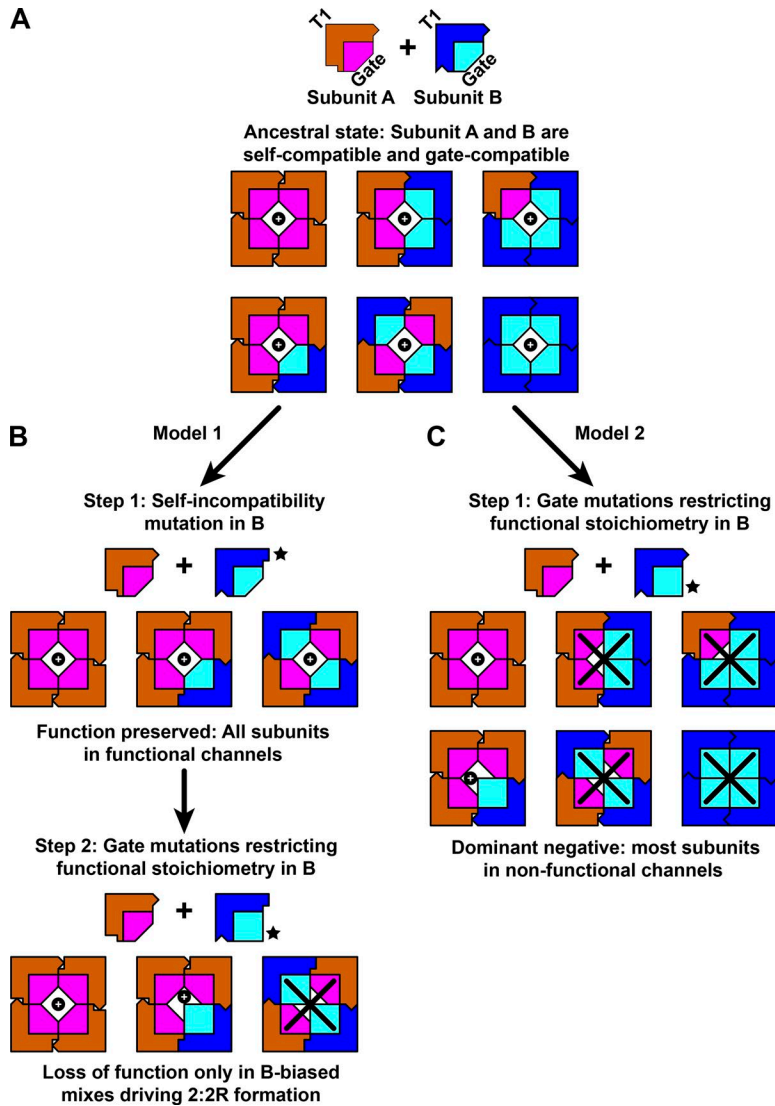
A

Subunit A   Subunit B

Ancestral state: Subunit A and B are self-compatible and gate-compatible

B   Model 1

Step 1: Self-incompatibility mutation in B

Function preserved: All subunits in functional channels

Step 2: Gate mutations restricting functional stoichiometry in B

Loss of function only in B-biased mixes driving 2:2R formation

C   Model 2

Step 1: Gate mutations restricting functional stoichiometry in B

Dominant negative: most subunits in non-functional channels

Figure 11. **Model for the evolution of Shaker-like Kv regulatory subunits adopting a 3:1R functional stoichiometry. (A)** A precondition for the evolution of the regulatory phenotype in Shaker-like Kv family channels is coexpression of two subunits (A and B) from the same subfamily (Kv1, Kv2, Kv3, or Kv4) in at least a subset of cells. Each subunit forms homomeric channels, and because they have cross-compatibility, they can also form heterotetramers in four possible stoichiometries (3A:1B, 2A:2B adjacent, 2A:2B diagonal, and 1A:3B). All channels formed are functional, indicated by the presence of a K$^+$ ion (black circle) in the pore. **(B)** Model 1, our favored model, provides a two-step path to evolution of the regulatory phenotype (in subunit B in this example) functioning in a 3:1R stoichiometry. In step 1, mutation(s) in subunit B establish self-incompatibility (shown here as mutations in T1, star), but do not eliminate cross-compatibility with subunit A. This restricts channel assembly to three possible stoichiometries (4A, 3A:1B, 2A:2B, diagonal); all assembled channels are functional. Expression of subunit B increases the number of channels formed (relative to expression of subunit A alone) and is therefore critical for maintaining currents at or near their premutation starting levels. Step 1 effectively established the regulatory phenotype for subunit B. In step 2 of the model, subunit B accumulates gate mutation(s) tolerated in only a single subunit (star), disrupting 2:2R assembly, conduction, or gating. This establishes 3:1R as the single functional heteromer stoichiometry. Loss of function in 2:2R channels is depicted by replacement of the K$^+$ ion with a black X. Dominant-negative suppression of current will occur at highly subunit B–biased expression ratios as few A-A contacts will form during assembly, but reasonable currents will remain with balanced expression. **(C)** In the alternative model 2, subunit B gate incompatibility (star) evolves first, while self-compatibility remains. This results in strong dominant negative suppression because most subunits are tied up in nonfunctional channels. Model 2 is likely an evolutionary dead end because the gate mutation will engage negative selection to preserve current levels.

propagate structural rearrangements broadly through the pore (Pau et al., 2017), the functional consequences of specific gate substitutions might vary significantly from channel to channel. The significance of the steric barrier observed in the Kv2.1:Kv6.4 2:2R model therefore requires experimental clarification. What the models do show is that the Kv6.4 gate will likely perturb pore structure, and that the degree of perturbation increases significantly when two Kv6.4 subunits participate in the gate formation (Fig. 10).

Because we were not able to reach 100% 2:2R formation with the Kv6.4-PIPIIV-Kv2.1CT or Kv6.4-Kv2.1T1-PIPIIV-Kv2.1CT chimeras even at highly biased expression ratios, regions of the channel other than T1 and the gate are also likely to play a role in suppression of the 2:2R stoichiometry. The inability of the Kv2.1 T1 to restore assembly of channels with more than two regulatory subunits in the Kv6.4-PIPIIV-Kv2.1CT background further suggests that other channel regions could also contribute to Kv6.4 self-incompatibility. A broader analysis of pore interface residues that differ between Kv2.1 and Kv6.4 might reveal additional factors limiting 2:2R formation. We focused on the gate here because of the consistent and striking evolutionary divergence of

the gate sequence among regulatory subunits (Fig. 2). It is also possible that 2:2R formation could be limited over the expression ratio range we tested if Kv2.1 simply has higher affinity for itself than Kv6.4, independent of any structural perturbations. We did not test higher expression ratios here because the concentrations of cRNA required compromised oocyte health. However, if Kv2.1 homodimerization is preferred to Kv2.1:Kv6.4 heterodimerization, our data suggest that the T1 domain alone does not account for the affinity difference because we were unable to increase 2:2R formation by substituting the Kv2.1 T1 into Kv6.4 or Kv6.4-PIPIIV-Kv2.1CT (Fig. 5 D). Furthermore, differential affinity does not contradict the role we found for the Kv6.4 gate in limiting 2:2R formation.

Based on the results presented here, we propose a two-step model for evolution of the regulatory phenotype in Shaker-like Kv family channels that predicts degeneration of the highly conserved activation gate sequence and opens an evolutionary path to a 3:1R stoichiometry (Fig. 11). In the first step, the regulatory phenotype, which is characterized by an inability to form homotetramers, is established by a self-incompatibility mutation, most likely in T1 as depicted here (Fig. 11 B). Both 3:1R

Pisupati et al.
Kv6.4 S6 gate influences K$^+$ channel stoichiometry

Journal of General Physiology
https://doi.org/10.1085/jgp.201812121

1718

and 2:2R stoichiometries are predicted to be functional because T1 self-incompatibility mutations are unlikely to affect channel function beyond assembly. The self-incompatible mutated channel produced in step 1 should remain under positive selection to maintain functional channel numbers. The original self-incompatibility mutation could in theory occur outside T1, provided it does not disrupt heteromer function. While the precise nature of the self-incompatibility mutation(s) in mammalian Kv2 subfamily regulatory subunits is not clear, the T1 is a likely spot because their T1 domains are self-incompatible (Salinas et al., 1997b; Kramer et al., 1998; Ottschytsch et al., 2002). Furthermore, a single amino acid change in the T1 of Kv1.3 is sufficient to create T1 self-incompatibility while preserving the ability to form heteromers with WT channels (Robinson and Deutsch, 2005). Nevertheless, our results indicate that Kv6.4 self-incompatibility extends beyond T1. Regardless of the location of the original step 1 mutation, self-incompatibility limits functional channels to no more than two mutated subunits/tetramer (Fig. 1). Selective pressure on the gate sequence is therefore reduced, and the gate can now accumulate mutations that can be functionally accommodated in no more than two subunits of a tetramer. In step 2 of the model, this evolutionary drift of the gate sequence over time could eventually result in mutations that are tolerated only in a single subunit, thus fixing the functional stoichiometry at 3:1R (Fig. 11 B). While some subunits in step 2 may be lost to nonfunctional stoichiometries, as we observe for Kv2.1:Kv6.4, advantageous new biophysical properties could maintain positive selection. The physiological advantage of a heteromeric delayed rectifier with a low activation threshold, slower kinetics, and closed state inactivation (Fig. 3) in neurons expressing Kv6.4 remains to be determined. We believe it is unlikely that evolution of the regulatory phenotype would begin with a restrictive gate mutation in step 1, because gate incompatibility in the presence of intact assembly would tie most of the expressed subunits up in nonfunctional tetramers (Fig. 11 C). The gate mutation would therefore serve as a strong dominant negative and would likely face immediate negative selection. This may help explain why the gate is so highly conserved in self-compatible homomer-forming Shaker-like Kv subunits.

This evolutionary model predicts the gate consensus sequence degeneration we observe in all independent evolutions of the regulatory subunit phenotype within the Shaker-like Kv family. A 3:1R stoichiometry could be the most likely long-term outcome because it is logical that the gate would eventually acquire a mutation that can be tolerated in only a single subunit. While maintenance of two functional stoichiometries might initially be selectively neutral, fixation on a single functional stoichiometry could gain a selective advantage over time as the regulatory subunit accumulates mutations that would functionally differentiate 3:1R from 2:2R channels. Nevertheless, the model does not require that each evolutionary instance of the regulatory subunit phenotype will fix at 3:1R, or that the observed regulatory subunit group will have reached a point of fixation. We believe 2:2R fixation should be less common because (a) the regulatory phenotype is most likely first established with a loss-of-function mutation in assembly, and (b) it is unlikely that any

gate mutations are better tolerated in a 2:2R configuration than a 3:1R configuration. Fixation on a 2:2R stoichiometry is possible within this model if this stoichiometry has unique, positively selected functional properties, but it might require secondary mutation(s) that favor heterodimer formation during assembly. Once a 2:2R stoichiometry is favored, gate mutations tolerated in only a single subunit would be selected against. A cnidarian Kv4 regulatory subunit jShalγ with only a single gate substitution (PVPIIQ) has been predicted to form functional channels in a 2:2R stoichiometry based on examination of the stoichiometry of N-type inactivation (Jegla and Salkoff, 1997), but in the absence of TIRF photobleaching analysis, it is unclear if 3:1R heteromers do or do not form.

Further functional characterization of independent evolutionary instances of regulatory subunits will be needed to test whether this model predictably describes the evolution of the regulatory subunit phenotype across the Shaker-like Kv family. It predicts that self-incompatibility should be a universal feature of regulatory subunits, and that an exclusive 3:1R functional stoichiometry should be common. It would also be interesting to see if there is correspondence between the predicted severity of gate mutations and regulatory subunit stoichiometry. Regardless, degeneration of the highly conserved activation gate sequence appears to have high predictive value for identifying evolution of the regulatory phenotype in Shaker-like Kv family. Another example of preferential assembly of a 3:1R stoichiometry in the voltage-gated cation channel superfamily is the heteromeric rod cyclic nucleotide-gated channels (Weitz et al., 2002; Zheng et al., 2002; Zhong et al., 2002). These channels lack the Shaker T1, but a cytoplasmic coiled-coil domain in the C terminus seems to play an analogous role; it is formed by three helices, one each contributed by the CNG1A subunits, while the regulatory CNGB1 is excluded and thus limited to a single subunit/channel. Our results suggest it would be interesting to look for coevolution of gate sequences and the regulatory phenotype across the breadth of the CNG channel family.

Acknowledgments

Pisupati et al.
Kv6.4 S6 gate influences K⁺ channel stoichiometry

Journal of General Physiology
https://doi.org/10.1085/jgp.201812121

1719

References

Anishkin, A., B. Akitake, K. Kamaraju, C.S. Chiang, and S. Sukharev. 2010. Hydration properties of mechanosensitive channel pores define the energetics of gating. *J. Phys. Condens. Matter.* 22:454120. https://doi.org/10.1088/0953-8984/22/45/454120

Beckstein, O., and M.S. Sansom. 2003. Liquid-vapor oscillations of water in hydrophobic nanopores. *Proc. Natl. Acad. Sci. USA.* 100:7063–7068. https://doi.org/10.1073/pnas.1136844100

Bocksteins, E., E. Mayeur, A. Van Tilborg, G. Regnier, J.P. Timmermans, and D.J. Snyders. 2014. The subfamily-specific interaction between Kv2.1 and Kv6.4 subunits is determined by interactions between the N- and C-termini. *PLoS One.* 9:e98960. https://doi.org/10.1371/journal.pone.0098960

Bocksteins, E., D.J. Snyders, and M. Holmgren. 2017. Independent movement of the voltage sensors in $K_V2.1/K_V6.4$ heterotetramers. *Sci. Rep.* 7:41646. https://doi.org/10.1038/srep41646

Carrasquillo, Y., and J.M. Nerbonne. 2014. IA channels: diverse regulatory mechanisms. *Neuroscientist.* 20:104–111. https://doi.org/10.1177/1073858413504003

Chen, Y., N.C. Deffenbaugh, C.T. Anderson, and W.O. Hancock. 2014. Molecular counting by photobleaching in protein complexes with many subunits: best practices and application to the cellulose synthesis complex. *Mol. Biol. Cell.* 25:3630–3642. https://doi.org/10.1091/mbc.e14-06-1146

Clancy, S.M., B. Chen, F. Bertaso, J. Mamet, and T. Jegla. 2009. KCNE1 and KCNE3 beta-subunits regulate membrane surface expression of Kv12.2 K(+) channels in vitro and form a tripartite complex in vivo. *PLoS One.* 4:e6330. https://doi.org/10.1371/journal.pone.0006330

Coste, B., B. Xiao, J.S. Santos, R. Syeda, J. Grandl, K.S. Spencer, S.E. Kim, M. Schmidt, J. Mathur, A.E. Dubin, et al. 2012. Piezo proteins are pore-forming subunits of mechanically activated channels. *Nature.* 483:176–181. https://doi.org/10.1038/nature10812

Covarrubias, M., A.A. Wei, and L. Salkoff. 1991. Shaker, Shal, Shab, and Shaw express independent K+ current systems. *Neuron.* 7:763–773. https://doi.org/10.1016/0896-6273(91)90279-9

Crooks, G.E., G. Hon, J.M. Chandonia, and S.E. Brenner. 2004. WebLogo: a sequence logo generator. *Genome Res.* 14:1188–1190. https://doi.org/10.1101/gr.849004

del Camino, D., and G. Yellen. 2001. Tight steric closure at the intracellular activation gate of a voltage-gated K(+) channel. *Neuron.* 32:649–656. https://doi.org/10.1016/S0896-6273(01)00487-1

del Camino, D., M. Kanevsky, and G. Yellen. 2005. Status of the intracellular gate in the activated-not-open state of shaker K+ channels. *J. Gen. Physiol.* 126:419–428. https://doi.org/10.1085/jgp.200509385

Dodson, P.D., M.C. Barker, and I.D. Forsythe. 2002. Two heteromeric Kv1 potassium channels differentially regulate action potential firing. *J. Neurosci.* 22:6953–6961. https://doi.org/10.1523/JNEUROSCI.22-16-06953.2002

Du, J., L.L. Haak, E. Phillips-Tansey, J.T. Russell, and C.J. McBain. 2000. Frequency-dependent regulation of rat hippocampal somato-dendritic excitability by the K+ channel subunit Kv2.1. *J. Physiol.* 522:19–31. https://doi.org/10.1111/j.1469-7793.2000.t01-2-00019.xm

Eswar, N., B. Webb, M.A. Marti-Renom, M.S. Madhusudhan, D. Eramian, M.Y. Shen, U. Pieper, and A. Sali. 2007. Comparative protein structure modeling using MODELLER. Curr Protoc Protein Sci. Chapter 2:Unit 2.9.

Hackos, D.H., T.H. Chang, and K.J. Swartz. 2002. Scanning the intracellular S6 activation gate in the shaker K+ channel. *J. Gen. Physiol.* 119:521–532. https://doi.org/10.1085/jgp.20028569

Humphrey, W., A. Dalke, and K. Schulten. 1996. VMD: visual molecular dynamics. J Mol Graph. 14:33–38, 27–38.

Jegla, T., and L. Salkoff. 1994. Molecular evolution of K+ channels in primitive eukaryotes. *Soc. Gen. Physiol. Ser.* 49:213–222.

Jegla, T., and L. Salkoff. 1997. A novel subunit for shal K+ channels radically alters activation and inactivation. *J. Neurosci.* 17:32–44. https://doi.org/10.1523/JNEUROSCI.17-01-00032.1997

Jegla, T., N. Grigoriev, W.J. Gallin, L. Salkoff, and A.N. Spencer. 1995. Multiple Shaker potassium channels in a primitive metazoan. *J. Neurosci.* 15:7989–7999. https://doi.org/10.1523/JNEUROSCI.15-12-07989.1995

Jegla, T., H.Q. Marlow, B. Chen, D.K. Simmons, S.M. Jacobo, and M.Q. Martindale. 2012. Expanded functional diversity of shaker K(+) channels in cnidarians is driven by gene expansion. *PLoS One.* 7:e51366. https://doi.org/10.1371/journal.pone.0051366

Jiang, Y., A. Lee, J. Chen, V. Ruta, M. Cadene, B.T. Chait, and R. MacKinnon. 2003. X-ray structure of a voltage-dependent K+ channel. *Nature.* 423:33–41. https://doi.org/10.1038/nature01580

Kerschensteiner, D., F. Soto, and M. Stocker. 2005. Fluorescence measurements reveal stoichiometry of K+ channels formed by modulatory and delayed rectifier alpha-subunits. *Proc. Natl. Acad. Sci. USA.* 102:6160–6165. https://doi.org/10.1073/pnas.0500468102

King, A.N., C.F. Manning, and J.S. Trimmer. 2014. A unique ion channel clustering domain on the axon initial segment of mammalian neurons. *J. Comp. Neurol.* 522:2594–2608. https://doi.org/10.1002/cne.23551

Kitaguchi, T., M. Sukhareva, and K.J. Swartz. 2004. Stabilizing the closed S6 gate in the Shaker Kv channel through modification of a hydrophobic seal. *J. Gen. Physiol.* 124:319–332. https://doi.org/10.1085/jgp.200409098

Kramer, J.W., M.A. Post, A.M. Brown, and G.E. Kirsch. 1998. Modulation of potassium channel gating by coexpression of Kv2.1 with regulatory Kv5.1 or Kv6.1 alpha-subunits. *Am. J. Physiol.* 274:C1501–C1510. https://doi.org/10.1152/ajpcell.1998.274.6.C1501

Kreusch, A., P.J. Pfaffinger, C.F. Stevens, and S. Choe. 1998. Crystal structure of the tetramerization domain of the Shaker potassium channel. *Nature.* 392:945–948. https://doi.org/10.1038/31978

Krovetz, H.S., H.M. VanDongen, and A.M. VanDongen. 1997. Atomic distance estimates from disulfides and high-affinity metal-binding sites in a K+ channel pore. *Biophys. J.* 72:117–126. https://doi.org/10.1016/S0006-3495(97)78651-X

Kumar, S., G. Stecher, and K. Tamura. 2016. MEGA7: Molecular Evolutionary Genetics Analysis Version 7.0 for Bigger Datasets. *Mol. Biol. Evol.* 33:1870–1874. https://doi.org/10.1093/molbev/msw054

Lau, D., E.C. Vega-Saenz de Miera, D. Contreras, A. Ozaita, M. Harvey, A. Chow, J.L. Noebels, R. Paylor, J.I. Morgan, C.S. Leonard, and B. Rudy. 2000. Impaired fast-spiking, suppressed cortical inhibition, and increased susceptibility to seizures in mice lacking Kv3.2 K+ channel proteins. *J. Neurosci.* 20:9071–9085. https://doi.org/10.1523/JNEUROSCI.20-24-09071.2000

Li, X., A. Anishkin, H. Liu, D.B. van Rossum, S.V. Chintapalli, J.K. Sassic, D. Gallegos, K. Pivaroff-Ward, and T. Jegla. 2015a. Bimodal regulation of an Elk subfamily K+ channel by phosphatidylinositol 4,5-bisphosphate. *J. Gen. Physiol.* 146:357–374. https://doi.org/10.1085/jgp.201511491

Li, X., H. Liu, J. Chu Luo, S.A. Rhodes, L.M. Trigg, D.B. van Rossum, A. Anishkin, F.H. Diatta, J.K. Sassic, D.K. Simmons, et al. 2015b. Major diversification of voltage-gated K+ channels occurred in ancestral parahoxozoans. *Proc. Natl. Acad. Sci. USA.* 112:E1010–E1019. https://doi.org/10.1073/pnas.1422941112

Li, X., A.S. Martinson, M.J. Layden, F.H. Diatta, A.P. Sberna, D.K. Simmons, M.Q. Martindale, and T.J. Jegla. 2015c. Ether-à-go-go family voltage-gated K+ channels evolved in an ancestral metazoan and functionally diversified in a cnidarian-bilaterian ancestor. *J. Exp. Biol.* 218:526–536. https://doi.org/10.1242/jeb.110080

Lien, C.C., and P. Jonas. 2003. Kv3 potassium conductance is necessary and kinetically optimized for high-frequency action potential generation in hippocampal interneurons. *J. Neurosci.* 23:2058–2068. https://doi.org/10.1523/JNEUROSCI.23-06-02058.2003

Liu, Y., M. Holmgren, M.E. Jurman, and G. Yellen. 1997. Gated access to the pore of a voltage-dependent K+ channel. *Neuron.* 19:175–184. https://doi.org/10.1016/S0896-6273(00)80357-8

Long, S.B., E.B. Campbell, and R. Mackinnon. 2005a. Crystal structure of a mammalian voltage-dependent Shaker family K+ channel. *Science.* 309:897–903. https://doi.org/10.1126/science.1116269

Long, S.B., E.B. Campbell, and R. Mackinnon. 2005b. Voltage sensor of Kv1.2: structural basis of electromechanical coupling. *Science.* 309:903–908. https://doi.org/10.1126/science.1116270

MacKerell, A.D., D. Bashford, M. Bellott, R.L. Dunbrack, J.D. Evanseck, M.J. Field, S. Fischer, J. Gao, H. Guo, S. Ha, et al. 1998. All-atom empirical potential for molecular modeling and dynamics studies of proteins. *J. Phys. Chem. B.* 102:3586–3616. https://doi.org/10.1021/jp973084f

MacKinnon, R. 1991. Determination of the subunit stoichiometry of a voltage-activated potassium channel. *Nature.* 350:232–235. https://doi.org/10.1038/350232a0

Malin, S.A., and J.M. Nerbonne. 2000. Elimination of the fast transient in superior cervical ganglion neurons with expression of KV4.2W362F: molecular dissection of IA. *J. Neurosci.* 20:5191–5199. https://doi.org/10.1523/JNEUROSCI.20-14-05191.2000

Malin, S.A., and J.M. Nerbonne. 2001. Molecular heterogeneity of the voltage-gated fast transient outward K+ current, I(Af), in mammalian neurons. *J. Neurosci.* 21:8004–8014. https://doi.org/10.1523/JNEUROSCI.21-20-08004.2001

Malin, S.A., and J.M. Nerbonne. 2002. Delayed rectifier K+ currents, IK, are encoded by Kv2 alpha-subunits and regulate tonic firing in mammalian sympathetic neurons. *J. Neurosci.* 22:10094–10105. https://doi.org/10.1523/JNEUROSCI.22-23-10094.2002

Martinson, A.S., D.B. van Rossum, F.H. Diatta, M.J. Layden, S.A. Rhodes, M.Q. Martindale, and T. Jegla. 2014. Functional evolution of Erg potassium

channel gating reveals an ancient origin for IKr. *Proc. Natl. Acad. Sci. USA.* 111:5712–5717. https://doi.org/10.1073/pnas.1321716111

Martí-Renom, M.A., A.C. Stuart, A. Fiser, R. Sánchez, F. Melo, and A. Sali. 2000. Comparative protein structure modeling of genes and genomes. *Annu. Rev. Biophys. Biomol. Struct.* 29:291–325. https://doi.org/10.1146/annurev.biophys.29.1.291

Misonou, H., D.P. Mohapatra, and J.S. Trimmer. 2005. Kv2.1: a voltage-gated k+ channel critical to dynamic control of neuronal excitability. *Neurotoxicology.* 26:743–752. https://doi.org/10.1016/j.neuro.2005.02.003

Mohapatra, D.P., D.F. Siino, and J.S. Trimmer. 2008. Interdomain cytoplasmic interactions govern the intracellular trafficking, gating, and modulation of the Kv2.1 channel. *J. Neurosci.* 28:4982–4994. https://doi.org/10.1523/JNEUROSCI.0186-08.2008

Murakoshi, H., and J.S. Trimmer. 1999. Identification of the Kv2.1 K+ channel as a major component of the delayed rectifier K+ current in rat hippocampal neurons. *J. Neurosci.* 19:1728–1735. https://doi.org/10.1523/JNEUROSCI.19-05-01728.1999

Nakajo, K., M.H. Ulbrich, Y. Kubo, and E.Y. Isacoff. 2010. Stoichiometry of the KCNQ1 - KCNE1 ion channel complex. *Proc. Natl. Acad. Sci. USA.* 107:18862–18867. https://doi.org/10.1073/pnas.1010354107

Ogawa, Y., I. Horresh, J.S. Trimmer, D.S. Bredt, E. Peles, and M.N. Rasband. 2008. Postsynaptic density-93 clusters Kv1 channels at axon initial segments independently of Caspr2. *J. Neurosci.* 28:5731–5739. https://doi.org/10.1523/JNEUROSCI.4431-07.2008

Ottschytsch, N., A. Raes, D. Van Hoorick, and D.J. Snyders. 2002. Obligatory heterotetramerization of three previously uncharacterized Kv channel alpha-subunits identified in the human genome. *Proc. Natl. Acad. Sci. USA.* 99:7986–7991. https://doi.org/10.1073/pnas.122617999

Ottschytsch, N., A.L. Raes, J.P. Timmermans, and D.J. Snyders. 2005. Domain analysis of Kv6.3, an electrically silent channel. *J. Physiol.* 568:737–747. https://doi.org/10.1113/jphysiol.2005.090142

Patel, A.J., M. Lazdunski, and E. Honoré. 1997. Kv2.1/Kv9.3, a novel ATP-dependent delayed-rectifier K+ channel in oxygen-sensitive pulmonary artery myocytes. *EMBO J.* 16:6615–6625. https://doi.org/10.1093/emboj/16.22.6615

Pathak, M.M., V. Yarov-Yarovoy, G. Agarwal, B. Roux, P. Barth, S. Kohout, F. Tombola, and E.Y. Isacoff. 2007. Closing in on the resting state of the Shaker K(+) channel. *Neuron.* 56:124–140. https://doi.org/10.1016/j.neuron.2007.09.023

Pau, V., Y. Zhou, Y. Ramu, Y. Xu, and Z. Lu. 2017. Crystal structure of an inactivated mutant mammalian voltage-gated K+ channel. *Nat. Struct. Mol. Biol.* 24:857–865. https://doi.org/10.1038/nsmb.3457

Pfaffinger, P.J., and D. DeRubeis. 1995. Shaker K+ channel T1 domain self-tetramerizes to a stable structure. *J. Biol. Chem.* 270:28595–28600. https://doi.org/10.1074/jbc.270.48.28595

Phillips, J.C., R. Braun, W. Wang, J. Gumbart, E. Tajkhorshid, E. Villa, C. Chipot, R.D. Skeel, L. Kalé, and K. Schulten. 2005. Scalable molecular dynamics with NAMD. *J. Comput. Chem.* 26:1781–1802. https://doi.org/10.1002/jcc.20289

Post, M.A., G.E. Kirsch, and A.M. Brown. 1996. Kv2.1 and electrically silent Kv6.1 potassium channel subunits combine and express a novel current. *FEBS Lett.* 399:177–182. https://doi.org/10.1016/S0014-5793(96)01316-6

Robinson, J.M., and C. Deutsch. 2005. Coupled tertiary folding and oligomerization of the T1 domain of Kv channels. *Neuron.* 45:223–232. https://doi.org/10.1016/j.neuron.2004.12.043

Rosenthal, J.J., R.G. Vickery, and W.F. Gilly. 1996. Molecular identification of SqKv1A. A candidate for the delayed rectifier K channel in squid giant axon. *J. Gen. Physiol.* 108:207–219. https://doi.org/10.1085/jgp.108.3.207

Roth, R., D. Gillespie, W. Nonner, and R.E. Eisenberg. 2008. Bubbles, gating, and anesthetics in ion channels. *Biophys. J.* 94:4282–4298. https://doi.org/10.1529/biophysj.107.120493

Rudy, B., and C.J. McBain. 2001. Kv3 channels: voltage-gated K+ channels designed for high-frequency repetitive firing. *Trends Neurosci.* 24:517–526. https://doi.org/10.1016/S0166-2236(00)01892-0

Sali, A., and J.P. Overington. 1994. Derivation of rules for comparative protein modeling from a database of protein structure alignments. *Protein Sci.* 3:1582–1596.

Salinas, M., J. de Weille, E. Guillemare, M. Lazdunski, and J.P. Hugnot. 1997a. Modes of regulation of shab K+ channel activity by the Kv8.1 subunit. *J. Biol. Chem.* 272:8774–8780. https://doi.org/10.1074/jbc.272.13.8774

Salinas, M., F. Duprat, C. Heurteaux, J.P. Hugnot, and M. Lazdunski. 1997b. New modulatory alpha subunits for mammalian Shab K+ channels. *J. Biol. Chem.* 272:24371–24379. https://doi.org/10.1074/jbc.272.39.24371

Sand, R.M., D.M. Atherton, A.N. Spencer, and W.J. Gallin. 2011. jShaw1, a low-threshold, fast-activating K(v)3 from the hydrozoan jellyfish Poly-orchis penicillatus. *J. Exp. Biol.* 214:3124–3137. https://doi.org/10.1242/jeb.057000

Shen, N.V., and P.J. Pfaffinger. 1995. Molecular recognition and assembly sequences involved in the subfamily-specific assembly of voltage-gated K+ channel subunit proteins. *Neuron.* 14:625–633. https://doi.org/10.1016/0896-6273(95)90319-4

Sukhareva, M., D.H. Hackos, and K.J. Swartz. 2003. Constitutive activation of the Shaker Kv channel. *J. Gen. Physiol.* 122:541–556. https://doi.org/10.1085/jgp.200308905

Trimmer, J.S. 2015. Subcellular localization of K+ channels in mammalian brain neurons: remarkable precision in the midst of extraordinary complexity. *Neuron.* 85:238–256. https://doi.org/10.1016/j.neuron.2014.12.042

Tsunoda, S., and L. Salkoff. 1995a. Genetic analysis of Drosophila neurons: Shal, Shaw, and Shab encode most embryonic potassium currents. *J. Neurosci.* 15:1741–1754. https://doi.org/10.1523/JNEUROSCI.15-03-01741.1995

Tsunoda, S., and L. Salkoff. 1995b. The major delayed rectifier in both Drosophila neurons and muscle is encoded by Shab. *J. Neurosci.* 15:5209–5221. https://doi.org/10.1523/JNEUROSCI.15-07-05209.1995

Tu, L., and C. Deutsch. 1999. Evidence for dimerization of dimers in K+ channel assembly. *Biophys. J.* 76:2004–2017. https://doi.org/10.1016/S0006-3495(99)77358-3

Ulbrich, M.H., and E.Y. Isacoff. 2007. Subunit counting in membrane-bound proteins. *Nat. Methods.* 4:319–321. https://doi.org/10.1038/nmeth1024

Upadhyay, A., A. Pisupati, T. Jegla, M. Crook, K.J. Mickolajczyk, M. Shorey, L.E. Rohan, K.A. Billings, M.M. Rolls, W.O. Hancock, and W. Hanna-Rose. 2016. Nicotinamide is an endogenous agonist for a C. elegans TRPV OSM-9 and OCR-4 channel. *Nat. Commun.* 7:13135. https://doi.org/10.1038/ncomms13135

Wang, W., and B.A. Malcolm. 1999. Two-stage PCR protocol allowing introduction of multiple mutations, deletions and insertions using QuikChange Site-Directed Mutagenesis. *Biotechniques.* 26:680–682. https://doi.org/10.2144/99264st03

Wang, H., D.D. Kunkel, T.M. Martin, P.A. Schwartzkroin, and B.L. Tempel. 1993. Heteromultimeric K+ channels in terminal and juxtaparanodal regions of neurons. *Nature.* 365:75–79. https://doi.org/10.1038/365075a0

Wang, L.Y., L. Gan, I.D. Forsythe, and L.K. Kaczmarek. 1998. Contribution of the Kv3.1 potassium channel to high-frequency firing in mouse auditory neurones. *J. Physiol.* 509:183–194. https://doi.org/10.1111/j.1469-7793.1998.183bo.x

Waterhouse, A.M., J.B. Procter, D.M. Martin, M. Clamp, and G.J. Barton. 2009. Jalview Version 2--a multiple sequence alignment editor and analysis workbench. *Bioinformatics.* 25:1189–1191. https://doi.org/10.1093/bioinformatics/btp033

Webster, S.M., D. Del Camino, J.P. Dekker, and G. Yellen. 2004. Intracellular gate opening in Shaker K+ channels defined by high-affinity metal bridges. *Nature.* 428:864–868. https://doi.org/10.1038/nature02468

Wei, A., M. Covarrubias, A. Butler, K. Baker, M. Pak, and L. Salkoff. 1990. K+ current diversity is produced by an extended gene family conserved in Drosophila and mouse. *Science.* 248:599–603. https://doi.org/10.1126/science.2333511

Weitz, D., N. Ficek, E. Kremmer, P.J. Bauer, and U.B. Kaupp. 2002. Subunit stoichiometry of the CNG channel of rod photoreceptors. *Neuron.* 36:881–889. https://doi.org/10.1016/S0896-6273(02)01098-X

Xu, J., W. Yu, Y.N. Jan, L.Y. Jan, and M. Li. 1995. Assembly of voltage-gated potassium channels. Conserved hydrophilic motifs determine subfamily-specific interactions between the alpha-subunits. *J. Biol. Chem.* 270:24761–24768. https://doi.org/10.1074/jbc.270.42.24761

Xue, T., E. Marbán, and R.A. Li. 2002. Dominant-negative suppression of HCN1- and HCN2-encoded pacemaker currents by an engineered HCN1 construct: insights into structure-function relationships and multimerization. *Circ. Res.* 90:1267–1273. https://doi.org/10.1161/01.RES.0000024390.97889.C6

Zhang, G., V. Gurtu, and S.R. Kain. 1996. An enhanced green fluorescent protein allows sensitive detection of gene transfer in mammalian cells. *Biochem. Biophys. Res. Commun.* 227:707–711. https://doi.org/10.1006/bbrc.1996.1573

Zheng, J., M.C. Trudeau, and W.N. Zagotta. 2002. Rod cyclic nucleotide-gated channels have a stoichiometry of three CNGA1 subunits and one CNGB1 subunit. *Neuron.* 36:891–896. https://doi.org/10.1016/S0896-6273(02)01099-1

Zhong, H., L.L. Molday, R.S. Molday, and K.W. Yau. 2002. The heteromeric cyclic nucleotide-gated channel adopts a 3A:1B stoichiometry. *Nature.* 420:193–198. https://doi.org/10.1038/nature01201

Zhu, X.R., R. Netzer, K. Böhlke, Q. Liu, and O. Pongs. 1999. Structural and functional characterization of Kv6.2 a new gamma-subunit of voltage-gated potassium channel. *Receptors Channels.* 6:337–350.